

1 **Effect of dust on rainfall over the Red Sea coast based on WRF-Chem model simulations**

2 Sagar P. Parajuli<sup>1\*</sup>, Georgiy L. Stenchikov<sup>1</sup>, Alexander Ukhov<sup>1</sup>, Suleiman Mostamandi<sup>1</sup>, Paul A.  
3 Kucera<sup>2</sup>, Duncan Axisa<sup>3</sup>, William I. Gustafson Jr.<sup>4</sup>, and Yannian Zhu<sup>5</sup>

4

5

6 <sup>1</sup>King Abdullah University of Science and Technology, Thuwal, Saudi Arabia

7 <sup>2</sup>National Center for Atmospheric Research, Boulder, CO 80305, USA

8 <sup>3</sup>Center for Western Weather and Water Extremes (CW3E), Scripps Institution of Oceanography,  
9 University of California, San Diego, La Jolla, California, USA

10 <sup>4</sup>Pacific Northwest National Laboratory (PNNL), Richland, WA 99354, USA

11 <sup>5</sup>School of Atmospheric Sciences, Nanjing University, 210023 Nanjing, China

12

13

14

15

16

17 \*Corresponding Author, E-mail: [sagar.parajuli@kaust.edu.sa](mailto:sagar.parajuli@kaust.edu.sa)

18 **Abstract**

19 Water is the single most important element of life. Rainfall plays an important role in the spatial  
20 and temporal distribution of this precious natural resource and it has a direct impact on  
21 agricultural production, daily life activities, and human health. One of the ~~main-important~~  
22 elements that govern rainfall formation and distribution is atmospheric aerosol, which also  
23 affects the Earth's radiation balance and climate. Therefore, understanding how dust  
24 compositions and distributions affects the regional rainfall pattern is of crucial, particularly in  
25 regions with high atmospheric dust loads such as the Middle East. Although aerosol and rainfall  
26 research has garnered increasing attention both as an independent and interdisciplinary topic in  
27 the last few decades, the details of various direct and indirect pathways by which dust affects  
28 rainfall are not yet fully understood. Here, we explored the effects of dust on rainfall formation  
29 and distribution as well as the physical mechanisms that govern these phenomena, using high-  
30 resolution WRF-Chem simulations ( $\sim 1.5 \times 1.5$  km) configured with an advanced double-moment  
31 cloud microphysics scheme coupled with a sectional 8-bin aerosol scheme. Our model-simulated  
32 results were realistic, as evaluated from multiple perspectives including vertical profiles of  
33 aerosol concentrations, aerosol size distributions, vertical profiles of air temperature, diurnal  
34 wind cycles, and spatio-temporal rainfall patterns. Rainfall over the Red Sea coast is mainly  
35 caused by warm rain processes, which are typically confined within a height of  $\sim 6$  km over the  
36 Sarawat mountains and exhibit a strong diurnal cycle that peaks in the evening at approximately  
37 6 pm local time under the influence of sea breezes. Numerical experiments indicated that dust  
38 could both suppress or enhance rainfall. The effect of dust on rainfall were calculated as total,  
39 indirect, and direct effects, based on 10-year August-average daily-accumulated rainfall over the  
40 study domain covering the eastern Red Sea coast. For extreme rainfall events (domain-average  
41 daily-accumulated rainfall of  $\geq 1.33$  mm), the net effect of dust on rainfall was positive or  
42 enhancement (6.05%), the indirect effect (4.54%) and direct effect (1.51%) both causing rainfall  
43 increase. At a 5% significance level, the total and indirect effects were statistically significant  
44 whereas the direct effect was not. For normal rainfall events (domain-average daily-accumulated  
45 rainfall  $< 1.33$  mm), the indirect effect enhanced rainfall (4.76%) whereas the direct effect  
46 suppressed rainfall (-5.78%), resulting in a negative net suppressing effect (-1.02%), all of which  
47 were statistically significant. For extreme rainfall events (domain average daily accumulated  
48 rainfall of  $\geq 1.33$  mm), the total (6.05%), indirect (4.54%), and direct effects (1.51%) were all  
49 positive (enhancement). At a 5% significance level, the total and indirect effects were  
50 statistically significant whereas the direct effect was not. For normal rainfall events (domain-  
51 average daily accumulated rainfall  $< 1.33$  mm), the indirect effect enhanced rainfall (4.76%)  
52 whereas the direct effect suppressed rainfall (-5.78%), resulting in a negative net suppressing  
53 effect (-1.02%), all of which were statistically significant. We investigated the possible physical  
54 mechanisms of the effects and found that the ~~rainfall suppression by dust~~ dust direct effects ~~were~~  
55 was mainly caused by the scattering ~~and absorption~~ of solar radiation by dust. The surface  
56 cooling (~~warming~~) induced by ~~dust scattering (absorption)~~ weakens (~~strengthens~~) the sea breeze  
57 circulation, which decreases (~~increases~~) the associated landward moisture transport, ultimately  
58 suppressing (~~enhancing~~) rainfall. For extreme rainfall events, dust causes net rainfall  
59 enhancement through indirect effects as the high dust concentration facilitates raindrops to grow  
60 when the water vapor is sufficiently available. Our results have broader scientific and

61 environmental implications. Specifically, although dust is considered a problem from an air  
62 quality perspective, our results highlight the important role of dust on sea breeze circulation and  
63 associated rainfall over the Red Sea coastal regions. Our results also have implications for cloud  
64 seeding and water resource management.

65 **1. Introduction**

66 Rainfall rejuvenates plant and animal life. In desert regions, rain events also bring hope and  
67 excitement. Rainfall affects the distribution of surface and ground water resources, which are  
68 constantly declining over the Middle East and North Africa (MENA) region due to  
69 overexploitation (Joodaki et al., 2014). A large proportion of global agricultural production is  
70 indeed dependent on monsoon rainfall. Irregular patterns of rainfall have affected people in many  
71 countries across the globe, by causing floods and droughts, affecting the regional water resources  
72 (e.g., Jha et al., 2021), limiting people’s access to safe drinking water, and increasing the  
73 prevalence of water-borne diseases such as malaria and diarrhea (Trinh et al., 2020).

74 Dust is the dominant aerosol type in desert regions (Kalenderski and Stenchikov, 2016; Parajuli  
75 et al., 2020; Ukhov et al., 2020) and it can affect regional water resources by modulating rainfall  
76 distributions (Jha et al., 2021). In regions with long-term water shortages such as the Middle East  
77 and North Africa (MENA), understanding the multifaceted aspects of dust-rainfall connections is  
78 even more important. In desert regions, regional dust storms such as haboobs (e.g., Anisimov et  
79 al., 2018) are often associated with rainfall. The older generation of people in the MENA region  
80 associate certain categories of dust storms with rainfall. Due to the frequent occurrence of dust  
81 storms, dust-cloud mixtures are common sights in this region.

82 Aerosol particles including dust are key to rainfall formation as they provide a surface for  
83 condensation. J. Aitken, a pioneer scientist of the 18th century, said, “There would probably be  
84 no rainfall if there were no dust particles in the atmosphere” (Spurny, 2000), which clearly  
85 highlights the importance of dust on the Earth’s climate.

86 The process of rainfall is incredibly complex and many aspects of the rain cycle remain unclear  
87 despite sustained research efforts. Although the principles that govern rainfall appear highly  
88 complex from a prediction perspective, the basic physics of rainfall are rather simple and  
89 mesmerizing. The least understood aspects of rainfall lie within the clouds, particularly the  
90 mechanisms by which aerosols affect clouds and the subsequent rainfall.

91 Given that the multiple effects of aerosols on the Earth’s climate occur through various direct  
92 and indirect pathways, disentangling their effect on rainfall is not easy. Furthermore, previous  
93 studies on the effects of aerosols on rainfall have reported contradicting results, with some  
94 indicating that dust enhances rainfall while others report a suppressing effect. Generally, aerosols  
95 enhance heavy rainfall events and suppress light rainfall events (Choobari, 2018; Li et al., 2011).  
96 Although multiple new mechanisms have been recently proposed to explain the underlying  
97 causes of these discrepancies (e.g., Fan et al. 2018; Grabowski and Morrison, 2020; Abott and  
98 Cronin, 2021), these hypotheses are still debated and at times controversial (Choobari, 2018)  
99 despite extensive research on the topic. Furthermore, the effect of dust depends on the type of  
100 circulation (e.g., Bangalath and Stenchikov, 2015), and therefore the present study is highly  
101 significant in the coastal areas where sea and land breeze circulations are active. In this work, we  
102 specifically focus on the coastal regions of the Red Sea to explore the effects of dust on rainfall.  
103 We chose this region because dust-rainfall interaction should be prominent here, if any, given the  
104 high levels of atmospheric dust in the region.

105 The effects of aerosol on climate are generally classified into three categories – direct, semi-  
106 direct, and indirect effects (Lohmann and Feichter, 2001; Forkel et al., 2012; Zeinab et al., 2020),  
107 all of which affect rainfall in unique ways. Aerosol particles directly affect radiation through  
108 scattering and absorption, which is generally known as the “direct aerosol effect.” These effects  
109 on radiation leads to changes in temperature, wind speed, relative humidity, and atmospheric  
110 stability, all of which are collectively referred to as aerosol “semi-direct effects” (Hansen, et al.,  
111 1997). Furthermore, the effects of aerosols through clouds are classified as indirect effects  
112 (Twomey, 1991), which in turn are sub-classified into two types. The formation of cloud  
113 condensation nuclei (CCN) or ice nuclei (IN) (Dennis, 1980; Stull, 2000) changes the cloud  
114 optical properties, particularly cloud albedo, and this is referred to as the “first indirect effect”  
115 (Kravitz et al., 2014). The subsequent changes in cloud cover, cloud lifetime and rainfall are  
116 referred to as the “second indirect effect” (Lohmann and Feichter, 2001). In the literature, these  
117 effects are commonly calculated in terms of “radiative forcing.” However, here, we calculate  
118 how these effects translate into rainfall amounts, to gain insights into the effects of dust on  
119 rainfall from a water resources perspective.

120 Dust can both increase and decrease rainfall by affecting local atmospheric circulation (Jacobson  
121 et al., 2006; Rémy et al., 2015). For example, in West Africa, dust can reduce rainfall by  
122 inducing a cooling effect that decreases the meridional gradient of moist static energy (Konare et  
123 al., 2008). In contrast, dust can also enhance rainfall through dust-induced diabatic warming in  
124 the upper troposphere, which enhances regional circulation (Jin et al., 2015) through the  
125 “elevated heat pump” (EHP) effect (Lau et al., 2010). Dust can act both as IN (Creamean et al.,  
126 2013; Jha et al., 2018), which mainly affect cold cloud processes (Ansmann et al., 2005), and  
127 CCN, which primarily affect warm cloud processes (Li et al., 2010; Twohy, 2015; Jha et al.,  
128 2018). Nucleation is more effective when the CCN are hydrophilic. Although dust particles are  
129 weakly hydrophilic, they are larger and are activated at a higher supersaturation compared to  
130 other anthropogenic aerosol species (Karydis et al., 2011).

131 Increases in aerosol concentration increase the number of cloud droplets by shifting the aerosol  
132 spectrum towards smaller radii for a fixed liquid water content, which ultimately renders the  
133 autoconversion or collision-coalescence process in warm clouds less efficient and increases the  
134 cloud reflectivity, thus inducing a cooling effect on the Earth’s surface (Albrecht, 1989;  
135 Choobari, 2018). Aerosol particles can reduce the cloud fraction by slowing down rain formation  
136 by collision/coalescence (Rosenfeld et al., 2000; Jacobson et al., 2006; Min et al., 2008) but they  
137 can also increase via the invigoration of convective clouds (Koren et al., 2005). Aerosol  
138 invigoration is a process in which aerosols delay the rainfall in the initial stage of convection but  
139 causes more rainfall in the mature stage due to the formation of deeper and larger clouds  
140 (Andreae et al., 2004; Koren et al., 2005; Koren et al., 2008; Chakraborty et al., 2018; Fan et al.,  
141 2018). The presence of fine aerosol particles in the atmosphere facilitates the formation of  
142 smaller cloud droplets and therefore suppresses rainfall initially. This suppression allows the  
143 cloud droplets to reach the freezing point as they rise to higher altitudes. Upon freezing, these  
144 hydrometeors release more latent heat, which ultimately intensifies convective updrafts and  
145 associated cold rainfall (Koren et al., 2008; Lee et al., 2011). One more reason for these  
146 contrasting effects is that the aerosols behave differently in different cloud types. For example, a

147 dust layer below a warmer cloud base at approximately 3 km can suppress cloud formation by  
148 heating, but in a higher cloud base, cloud formation can be strengthened through the contribution  
149 of CCN/IN (Yin and Chen, 2007). Similarly, the effective radius of ice particles decreases with  
150 increased aerosol optical depth (AOD) in high clouds, whereas it increases for low clouds (Zhao  
151 et al., 2019). The rainfall response also depends on whether clouds are located over the continent  
152 or the ocean (Yin et al., 2002), or whether they are located over pristine remote areas or hazy  
153 urban regions (Solomos et al., 2011).

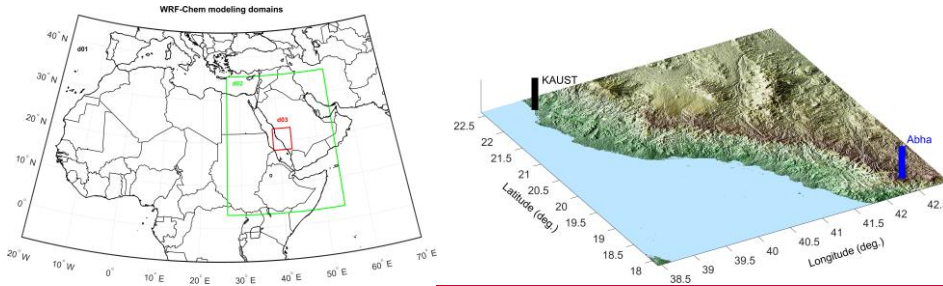
154 In summary, the effects of aerosol or dust on rainfall are governed by multiple microphysical,  
155 dynamic and radiative interactions, which can either suppress, enhance, or cause no net effect on  
156 rainfall depending on the regional geography (Andreae et al., 2004; Han et al., 2009). Therefore,  
157 regional modeling approaches (e.g., Konare et al., 2008; Zhang et al., 2017; Jordan et al., 2020)  
158 are necessary to understand the regional effects of dust on rainfall. Our study focused on the Red  
159 Sea Arabian coast, which is among the regions with the highest moisture transport, and where  
160 both natural (dust) and anthropogenic aerosols exist in high concentrations. Using the Weather  
161 Research Forecast model coupled with Chemistry (WRF-Chem) (Grell et al., 2005) model  
162 simulations supported by extensive validation of meteorology, aerosol properties, and  
163 microphysical parameters, our study aimed to understand the following research questions:

- 164 1. Does dust enhance or suppress rainfall? What physical mechanisms are responsible for  
165 any enhancement or suppression effect?
- 166 2. How does dust interact with local breeze circulations?

## 167 **2. Methods**

### 168 **2.1. Study domain**

169 Our study was conducted in a small domain over the Red Sea coast, as indicated by the red box  
170 (d03) in Fig. 1. The study area covers the King Abdullah University of Science and Technology  
171 (KAUST), Thuwal, in the north and the city of Abha in the south, the latter of which is famous  
172 for its high mountains and rainfall. The domain covers a full section of the Red Sea, the Sarawat  
173 Mountain range that runs from north to south, and a good portion of the nearby inland deserts  
174 (d03). The study domain is encompassed by a middle domain d02, which covers a large part of  
175 the Arabian Peninsula and northeast Africa, where major dust exchange occurs between the two  
176 continents across the Red Sea (Kalenderski and Stenchikov, 2016). The outer domain d01, which  
177 is rather large, covers the entire MENA region and includes all regional aerosol sources, as  
178 described in Parajuli et al., 2020.



Formatted: Font: Bold, Complex Script Font: Bold

179

180 Figure 1. Study area over the Red Sea coast (d03). WRF-Chem model simulations were  
 181 conducted showing using the nested domains d01, d02, and d03 used to conduct WRF-Chem  
 182 model simulations (left), and a zoom in topographic map of the domain d03 over the Red Sea  
 183 coast (right).

184 Precipitation over the Red Sea coast is governed by the complex interactions between sea  
 185 breezes, local topography, and upper-level thermodynamics (Kucera et al., 2010). A moisture  
 186 convergence boundary is created when the moist air from the sea (driven by sea breezes) that is  
 187 orographically lifted along the mountain slope meets the dry Harmattan winds originating from  
 188 the desert, which induces convective cloud development (Kucera et al., 2010; Parajuli et al.,  
 189 2020).

190 Land and sea breezes (Simpson, 1994; Miller et al., 2003) are key components of the local  
 191 atmospheric circulation that affect the rainfall pattern over the Red Sea coast. During the  
 192 daytime, the coastal plains of the Red Sea become warmer, thus creating a pressure low. The  
 193 moisture-laden air from the Red Sea then flows towards the low-pressure region, giving rise to  
 194 sea breezes (Khan et al., 2015; Parajuli et al., 2020). At nighttime, the land cools down often  
 195 below the sea surface temperature particularly during the winter, which drives land breezes that  
 196 flow from the land to the sea (Parajuli et al., 2020).

## 197 2.2. Observations

198 Our study employed rainfall data from a recently developed algorithm called the Integrated  
 199 Multi-satellite Retrievals (IMERG) for Global Precipitation Measurement (GPM), which  
 200 combines data from the GPM constellation with the earlier precipitation estimates from TRMM  
 201 (Tropical Rainfall Measurement Mission) (Liu et al., 2012) to increase coverage, accuracy, and  
 202 resolution (Huffman, et al., 2019). We specifically used the level-3 gauge-calibrated multi-  
 203 satellite precipitation estimate (PrecipitationCal) V06 dataset available daily at a spatial  
 204 resolution of  $0.1^\circ \times 0.1^\circ$ .

205 Additionally, our study used Moderate Resolution Imaging Spectroradiometer (MODIS) level-2  
 206 Deep Blue AOD data (Hsu et al., 2004), which are available daily for the whole globe, at a  
 207 resolution of  $\sim 0.1^\circ \times 0.1^\circ$ . We used the MODIS AOD collection 6 dataset (Hsu et al., 2013),  
 208 which features an improved Deep Blue aerosol retrieval algorithm. Data analyses were

209 conducted using the daily average AOD from the Terra and Aqua satellites, which encompassed  
210 measurements at ~10:30 am and ~1:30 pm local time, respectively.

211 Model comparisons were also conducted using the aerosol optical depth (AOD) from Aerosol  
212 Robotic Network (AERONET) (Holben et al., 1998) and aerosol vertical profiles from  
213 micropulse lidar (MPL) (Parajuli et al., 2020; Lopatin et al., 2021), both from the KAUST station  
214 (22.3N, 39.1E). We used cloud-screened and quality-assured level-2 AERONET AOD data,  
215 which were retrieved using the direct sun algorithm. We also use AERONET V3, level-2 aerosol  
216 number density and particle size distribution (PSD), which were obtained by inversion (Dubovik  
217 et al., 2000) and provides volume concentrations in 22 bins between a 0.05 and 15 micron radius  
218 (e.g., Parajuli et al., 2019). The LIDAR aerosol vertical profiles were retrieved using the GRASP  
219 algorithm following a multi-pixel approach that allows both daytime and nighttime retrievals  
220 with the use of collocated AERONET data (Dubovik et al., 2011; Parajuli et al., 2020; Lopatin et  
221 al., 2020).

222 Modern-Era Retrospective Analysis for Research and Applications version 2 (MERRA-2) data  
223 (Rienecker et al., 2011) were also used for model comparison.

224 Wind speed data from the KAUST station (Farrar et al., 2009) and radiosonde temperature data  
225 were obtained from King Abdul Aziz International Airport, Jeddah (41024-OEJN: 21.70N,  
226 39.18E) available from: <http://weather.uwyo.edu/upperair/sounding.html>.

227 CCN number concentrations were retrieved from VIIRS data following the Automated Mapping  
228 of Convective Clouds (AMCC) algorithm (Yue et al., 2019) to validate our model results. The  
229 algorithm extends the novel idea proposed by Rosenfeld et al. (2012) to simultaneously retrieve  
230 the CCN concentrations and the cloud base updraft speeds using visible and infrared satellite  
231 data. The number of activated CCN in a convective cloud base can be calculated as a function of  
232 cloud drop effective radius (varies with altitude as in an adiabatic cloud), which can be retrieved  
233 from a satellite imager with high-resolution wave bands such as the VIIRS (Visible Infrared  
234 Imaging Radiometer Suite) onboard the Suomi NPP (National Polar-Orbiting Satellite) (Freud et  
235 al., 2011; Rosenfeld et al., 2012; Rosenfeld et al., 2014). Similarly, the cloud base updraft speeds  
236 can be estimated as a linear function of cloud-base height (Zheng and Rosenfeld, 2015;  
237 Rosenfeld et al., 2016; Yue et al., 2019).

238 After identifying the convective cloud cells, the CCN number concentrations from the VIIRS  
239 satellite were retrieved corresponding to different cloud base heights (~0.5–5.5 km) representing  
240 different locations and times, which resulted in 14 days of data availability in August 2015. For  
241 comparison, we first extracted the CCN concentrations for each of the 14 days of satellite  
242 observations closest to the measurement time from the hourly model output. Next, the 3-d model  
243 data were interpolated along the latitude, longitude, and altitude (cloud base) of the satellite data  
244 points. The satellite data represented a range of supersaturations, and therefore only the data that  
245 fell within the modeled supersaturation range (0.02–1.0%) were extracted for further processing.  
246 The model CCN number concentrations were available at supersaturations of  $S = 0.02, 0.05, 0.1,$   
247  $0.2, 0.5,$  and  $1.0\%$ , therefore, for comparison, the model CCN concentrations at the points of



248 satellite-retrieved supersaturations were obtained by fitting a 3<sup>rd</sup> order polynomial on the model  
249 concentrations vs. supersaturations plot at the six model points.

250 We also used CCN number concentrations measured using a Droplet Measurement Technologies  
251 (DMT) CCN counter (Roberts and Nenes, 2005) during a field campaign in the Abha region of  
252 Saudi Arabia in August 2009 (Kucera et al., 2010). CCN number concentrations were measured  
253 at a PME (Presidency of Meteorology and Environment) ground station (18.24N, 42.46E) using  
254 a CCN counter (1–10 micron) at multiple supersaturations ( $S = 0.2$  and  $0.7\%$  were used for  
255 comparison in this study). The model CCN number concentrations at the observation points of  $S$   
256  $= 0.2$  and  $0.7\%$  were obtained by fitting a 3<sup>rd</sup> order polynomial equation on the model  
257 concentrations corresponding to the six model supersaturations, as mentioned previously.

258 Size-resolved aerosol concentrations were collected from a research aircraft (A Beechcraft King  
259 Air B200) during the field campaign (August 2009) with multiple probes including a Particle  
260 Measuring Systems (PMS) Forward Scatter Spectrometer Probe (FSSP-100, range 3,  $0.5\text{--}8\ \mu\text{m}$   
261 diameter) (Dye and Baumgardner, 1984) and a Passive Cavity Aerosol Spectrometer Probe  
262 (PCASP) ( $0.1\text{--}3\ \mu\text{m}$  diameter) (Kucera et al., 2010). For particle size comparisons, model data  
263 were averaged within the range of flight times (06:00 to 10:00 UTC) during the flight days  
264 (August 11–30, 2009). The model aerosol concentrations at the exact observation point along the  
265 flight track with a given latitude, longitude, and altitude were determined via 3-d linear  
266 interpolation of the model grid data.

## 267 **2.3. Model simulations**

### 268 **2.3.1. WRF-Chem model set-up**

269 High-resolution simulations are usually conducted for several days or weeks due to their high  
270 computational demand. Simulating full-scale aerosol-climate interactions including indirect  
271 effects adds further computational burdens. Therefore, considering our purpose, we conducted  
272 our model simulations using WRF-Chem at a cloud resolving spatial resolution of  $1.5\times 1.5\ \text{km}$   
273 for an entire month (August), of which the first three days were excluded from data analysis  
274 discarded for sas the spin-up period. Most model evaluations and diagnostic calculations were  
275 performed for a reference year (August 2015) unless otherwise mentioned. Additional  
276 validations are carried out for August 2009 because aerosol size distributions and microphysical  
277 data from a field campaign were available during this period.

278 To obtain statistically meaningful calculations of the dust effect on rainfall, 10 years of  
279 simulations (2006–2015) were conducted specifically for August of each year. The simulations  
280 were conducted over the Red Sea coast outlined by the nested domain d03 (Fig. 1), in which the  
281 parent domains d02 ( $4.5\times 4.5\ \text{km}$ ) and d01 ( $13.5\times 13.5\ \text{km}$ ) cover the Arabian Peninsula/northeast  
282 Africa and the MENA region, respectively. August was chosen because during this month the  
283 Red Sea coast receives abundant rainfall and sea breezes are relatively strong, which plays an  
284 important role in moisture transport over the coastal plains (Mostamandi et al., 2021).

285 We use 6-hourly ECMWF operational data (F640) as initial and boundary conditions, which is  
286 one of the most accurate reanalysis data assimilating several observations. The sea surface

287 ~~temperature (SST) was also updated every 6 hours using the skin temperature field from the~~  
288 ~~same ECMWF dataset. We continue to use this data because it has worked well in our region~~  
289 ~~(e.g., Parajuli et al., 2020; Mostamandi et al., 2022). The initial and lateral boundary conditions~~  
290 ~~were obtained from European Centre for Medium-Range Weather Forecasts (ECMWF)~~  
291 ~~operational analysis 6-hourly data downloaded at P640 Gaussian grids (~15 km). The sea surface~~  
292 ~~temperature (SST) was also updated every 6 hours using the skin temperature field from the~~  
293 ~~same ECMWF dataset.~~

294 To better represent cloud processes, it is important to use well-developed aerosol chemistry and  
295 microphysical schemes (Zhang et al., 2016). Here, we adopted the Model for Simulating Aerosol  
296 Interactions and Chemistry (MOSAIC) scheme (Fast et al., 2006; Zaveri et al., 2008; Zhao et al.,  
297 2011) with eight sectional aerosol bins. The MOSAIC scheme is computationally intensive and  
298 generates large outputs, as all aerosol concentrations are reported for the eight MOSAIC bins for  
299 interstitial and in-cloud aerosols. Our simulations used chem\_opt = 10, which couples the CBMZ  
300 (carbon bond mechanism) gas phase chemical mechanism (Zaveri and Peters, 1999) with the  
301 MOSAIC aerosol scheme, and is one of the most developed chemical mechanisms within WRF-  
302 Chem.

303 MOSAIC includes both interstitial and cloud-borne aerosols, cloud-aerosol interactions,  
304 activation/resuspension, nucleation, coagulation, aqueous chemistry, and wet removal (Fast et  
305 al., 2006; Gustafson et al., 2007). Here, we particularly focused on accurately representing dust  
306 aerosols because it is a specific ~~driving force in~~ characteristic of the region. MOSAIC includes all  
307 aerosols of interest including dust (included in other inorganic aerosols or “oin” because it is  
308 chemically inert), sea salt, sulfate, BC, and OC (Zhao et al., 2011; Zaveri et al., 2008). Within  
309 our model setup, aerosols affect clouds and clouds also affect aerosols, e.g., through in-cloud  
310 scavenging and by forming sulfate aerosols (Yang et al., 2012). Aerosol particles are assumed to  
311 be internally mixed and Köhler’s theory is used to relate the aerosol size distribution and  
312 composition to the activated CCN as a function of the maximum supersaturation (Abdul-Razzak  
313 and Ghan, 2002; Yang et al., 2012). Aerosol activation from the interstitial to in-cloud state is  
314 calculated based on a maximum supersaturation determined from a Gaussian spectrum of updraft  
315 velocities and internally mixed aerosol properties within each size bin (Chapman et al., 2009).  
316 When the hydrometeors evaporate, particles return to the original interstitial phase (Yang et al.,  
317 2012).

318 In MOSAIC, dust is treated as part of the internal mixture used across all aerosol species. All gas  
319 and aerosol processes (e.g., sulfate formation) operate within the mixture but dust itself does not  
320 take part in the chemical reactions, although MOSAIC includes the chemical reaction of CaCO<sub>3</sub>  
321 (a constituent of dust) with acids when the proportion of CaCO<sub>3</sub> is provided (Zaveri et al., 2008).  
322 Dust itself is considered weakly hydrophilic in WRF-Chem with a hygroscopicity of 0.14  
323 (Kawecki and Steiner, 2018). However, chemical processes within the aerosol mixture may  
324 affect the activation of CCN/IN, which ultimately affects precipitation (Abdelkader et al., 2017;  
325 Klingmüller et al., 2019). This is because interstitial aerosols are partially activated as CCN (in-  
326 cloud or cloud-borne aerosols) at each grid cell and time step by using a volume-weighted bulk  
327 hygroscopicity from all aerosol species (e.g., dust, sulfate, oin, sea salt) within each size bin

328 (Kawecki and Steiner, 2009; Tuccella et al., 2015) as a function of the environmental  
 329 supersaturation (Abdul-Razzak & Ghan, 2000). Reduction due to chemical and physical (e.g.,  
 330 coagulation) processes, as well as particle growth, will also cause particles to shift across  
 331 different bins (Abdul-Razzak and Ghan, 2002; Chapman et al., 2009). The volume-average  
 332 refractive index within a given size bin is used to calculate the optical properties using Mie  
 333 theory (Tuccella et al., 2015). Therefore, dust can affect both direct and indirect aerosol  
 334 feedback.

335 For cloud microphysics, we used the Morrison double-moment scheme (Morrison et al., 2009),  
 336 which is one of the commonly used microphysics options in WRF. This scheme allows for the  
 337 prognostic treatment of two moments of the hydrometeors (mixing ratios and number  
 338 concentrations) for five species (cloud droplets, cloud ice, snow, rain, and graupel), while  
 339 calculating key microphysical processes such as autoconversion, collection between hydrometeor  
 340 species, melting/freezing, and mass transfer from snow to ice (Yang et al., 2011). Compared to  
 341 the single-moment scheme, which only predicts mixing ratios, the double-moment approach can  
 342 better represent precipitating convective clouds particularly during heavy precipitation episodes  
 343 (Lim et al., 2010). The size distribution of hydrometeors is prescribed from the predicted bulk  
 344 number and mass mixing ratios of different hydrometeor types in an assumed gamma size  
 345 distribution (Gao et al., 2016). The prognostic treatment of the CCN distribution improves the  
 346 simulated cloud properties and radiative effects compared to a prescribed uniform CCN  
 347 distribution, albeit at an increased computational cost (Gustafson et al., 2007). The physics and  
 348 chemistry namelist options used in our WRF-Chem set up is summarized in Table 1.

349

350 Table 1. Physics and chemistry namelist settings used in WRF-Chem.

<b>Description</b>	<b>Namelist Options</b>	<b>References</b>
<b>Physics</b> Microphysics	mp_physics = 10	Morrison double-moment scheme (Morrison et al., 2009)
Planetary Boundary Layer (PBL) scheme	bl_pbl_physics = 1	Yonsei University Scheme (YSU) (Hong, et al., 2006)
Surface layer physics	sf_sfclay_physics = 1	Revised MM5 Monin-Obukhov scheme (Jimenez, renamed in v3.6)
Land Surface Model	sf_surface_physics = 2	Unified Noah land surface model (Tewari et al., 2004)
Cumulus parameterization	cu_physics = 0 (turned off)	
Radiative transfer model	ra_lw_physics = 4, ra_sw_physics = 4	Rapid Radiative Transfer Model (RRTMG) for both shortwave and longwave (Iacono et al., 2008)
<b>Chemistry</b> Chemistry option	chem_opt = 10 (8)	CBMZ chemical mechanism with MOSAIC 8-bin sectional aerosol scheme (MOSAIC 8-bin aerosol scheme)

Dust scheme	dust_opt = 13	GOCART dust emission scheme coupled with MOSAIC aerosol scheme
Photolysis scheme	phot_opt = 1	Madronich photolysis (TUV)

351 We included sea salt emissions using a parameterization based on 10-m wind speed (Monahan et  
352 al. 1986; Gong, 2003). Anthropogenic aerosol emissions were also included in our simulations.  
353 The emission of sulfur dioxide (SO<sub>2</sub>), which chemically transforms to sulfate aerosols, is  
354 prescribed using OMI (ozone monitoring instrument)-HTAP (Task Force Hemispheric Transport  
355 Air Pollution) data (Janssens-Maenhout et al., 2015) for 2015 developed by the National  
356 Aeronautics and Space Administration (NASA), as in Parajuli et al., 2020. Other emissions  
357 including BC and OC as well as SO<sub>2</sub> ship emissions are prescribed using the EDGAR (Emission  
358 Database for Global Atmospheric Research) database v4.3.2 available at a 0.1° × 0.1° resolution  
359 (Crippa et al., 2018).

360 The cloud-aerosol interactions on shortwave (SW) radiation are represented by linking the cloud  
361 droplet number concentration predicted by the microphysics scheme with the RRTMG  
362 shortwave radiative scheme. Aerosol direct radiative effects through longwave (LW) are also  
363 calculated using the RRTMG scheme (Iacono et al., 2000; Zhao et al., 2011). Aerosol indirect  
364 effects are calculated following Gustafson et al. (2004) to include both first and second indirect  
365 effects. Aerosol particles acting as CCN are coupled with the Morrison microphysics scheme,  
366 which allows aerosols to affect the cloud droplet number and cloud radiative properties, while  
367 also allowing clouds to alter aerosol size and composition through aqueous processes and wet  
368 scavenging (Gustafson et al., 2004). Note that we explicitly resolved the updrafts using a cloud-  
369 resolving spatial resolution in the inner domain (d03).

370 In MOSAIC, aerosol emissions are independently calculated within its own module in which the  
371 dust emission is calculated using the original GOCART dust scheme (Ginoux et al., 2001) as  
372 described by Zhao et al. (2010), which is called by setting dust\_opt = 13. Note that this option  
373 was not implemented in the version of WRF-Chem used herein (3.8.1), but we ported this change  
374 into our setup (within the subroutine module\_mosaic\_addemiss.F). We also accounted for  
375 gravitational settling of aerosols in this work similar to Ukhov et al. (2021), which has not been  
376 implemented for the MOSAIC scheme in WRF-Chem.

377 To represent dust sources, we used the topographic source function developed by Ginoux et al.  
378 (2001), which is calibrated to match the simulated AOD with observed AOD as in Parajuli et al.  
379 (2020). To accurately simulate the effect of dust on cloud formation and rainfall, it is important  
380 to ensure that the simulated AOD is consistent with the observations. The AOD is highly  
381 sensitive to the size distribution of the dust particles (Ukhov et al., 2021). Therefore, we  
382 iteratively adjusted the emission size distribution to match the volume size distribution of  
383 aerosols obtained from AERONET as described by Ukhov et al. (2020). There are two places in  
384 which the dust size distributions can be adjusted within WRF-Chem. First is the size distribution  
385 of the “emitted dust” prescribed in five bins within the GOCART dust scheme, which is  
386 specified in phys/module\_data\_gocart\_dust.F. The second is the dust size fractions used by the  
387 MOSAIC aerosol scheme (8 bins) specified in chem/module\_mosaic\_addemiss.F. Both of these

Formatted: Space Before: 8 pt

388 size fractions were modified to obtain a closer fit to the AERONET volume size distributions.  
 389 The modified and the default size fractions are presented in Table S1 and S2.

### 390 2.3.2. Experiments

391 Designing an appropriate experiment to determine the effect of dust in a model is challenging.  
 392 For example, one can consider a ‘baseline’ simulation with ‘clear’ conditions without any  
 393 aerosols and then add dust to see how it affects the rainfall. However, ‘clear’ conditions are  
 394 hardly ever observed and thus it is unrealistic to design an experiment with zero rainfall.  
 395 Therefore, we first considered a real-world scenario as a baseline by including all aerosols (dust,  
 396 sea salt, sulfate, organic, and black carbon) similar to Klingmüller et al. (2019), ~~in which the~~  
 397 ~~resulting rainfall closely matches the observed rainfall pattern~~ (Table 2, F1). This baseline  
 398 experiment (all\_aer) is calibrated against MODIS/AERONET AOD data by changing the dust  
 399 emission fractions and dust size fractions as mentioned previously in section 2.3.1. The results of  
 400 this baseline simulation were compared against observations, and thus which exhibited a realistic  
 401 aerosol distribution in terms of optical depth, PSD, and vertical profiles, as well as the rainfall  
 402 pattern (see section 3.2.1). The second experiment is the ‘no\_dust’ experiment (Table 2, F2) in  
 403 which we assigned ‘zero’ values to the source function in the dust emission equation (Parajuli et  
 404 al., 2019), thereby effectively eliminating dust emissions from all grid cells in all three domains.  
 405 Both of the aforementioned experiments include aerosol-radiation, aerosol-cloud, and  
 406 microphysical interactions, and therefore they represent the total effect (both direct and indirect)  
 407 of aerosols. From a practical perspective, the all\_aer experiment represents a ‘real world’  
 408 scenario in which all aerosols including dust are included to obtain a realistic rainfall pattern,  
 409 whereas the no\_dust experiment represents rainfall in an idealized, dust-free world. We also  
 410 conducted two additional experiments (F3 and F4) to separate the aerosol direct effects from  
 411 indirect effects. In these two simulations, we restricted aerosol-radiation interactions  
 412 (aer\_rad\_feedback = 0), both in all\_aer (F3) and no\_dust (F4) cases, while keeping all the model  
 413 physics and domain settings the same as in the previous two experiments. Therefore, these latter  
 414 two experiments essentially represent the indirect effects only.

415 The total effect ( $\Delta_{Tot}$ ), indirect effect ( $\Delta_{Indir}$ ), and direct effect ( $\Delta_{dir}$ ) of dust were then calculated  
 416 with the following equations:

$$417 \Delta_{tot} = F1 - F2 \quad (1)$$

$$418 \Delta_{indir} = F3 - F4 \quad (2)$$

$$419 \Delta_{dir} = \Delta_{Tot} - \Delta_{Indir} = (F1 - F2) - (F3 - F4) \quad (3)$$

420 Table 2. WRF-Chem model experiments

Aerosol species	Experiments with both direct and indirect effects		Experiments with indirect effects only		Experiments with direct effects only <sup>a</sup>		Experiments with direct effects only but without shortwave dust absorption <sup>b</sup>	
	F1 all_aer	F2 no_dust	F3 all_aer, no_direct	F4 no_dust, no_direct	F5 all_aer, no_indirect	F6 no_dust, no_indirect	F7 all_aer, no_indirect, no_absorb	F8 no_dust, no_indirect, no_absorb
Dust	yes	no	yes	no	yes	no	yes	no

Sea salt	yes	yes	yes	yes	yes	yes	yes	yes
Anthropogenic (sulfate, OC, and BC)	yes	Yes	yes	Yes	yes	Yes	yes	Yes

421 <sup>a, b</sup> diagnostic experiments (see section 3.3.2).

422 The physical processes through which dust affects breezes are difficult to understand when both  
423 direct and indirect effects are active. Additionally, the indirect effects are more complex and  
424 their representation in the model is accompanied by a high degree of uncertainty. For these  
425 reasons, we additionally analyzed the direct effects of dust alone from an independent pair of  
426 simulations involving the dust direct effects only (F5, F6, Table 2) [i.e., without considering the  
427 indirect effects (chem\_opt = 8)].

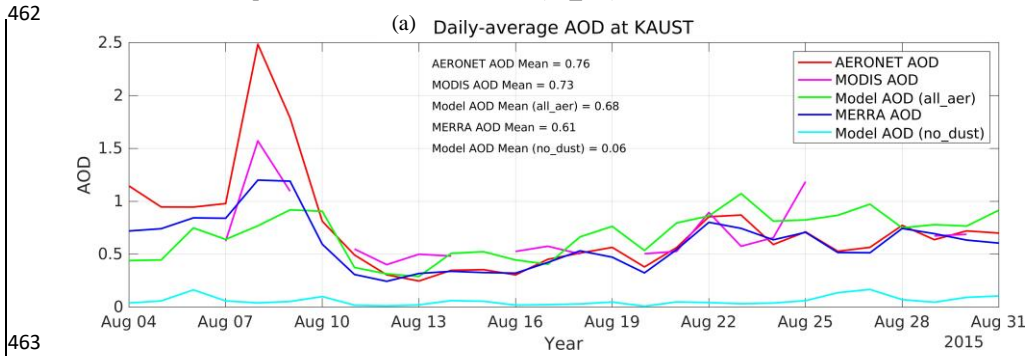
428 The dust direct effect is caused by both scattering and absorption of radiation in the SW bands.  
429 Therefore, to further understand the relative importance of shortwave cooling and warming  
430 resulting from direct effects, we conducted an additional pair of simulations (F7, F8, Table 2), in  
431 which we restricted the shortwave absorption of radiation by dust in the previous experiments F5  
432 and F6. To achieve this, we changed the imaginary part of the refractive index for dust from the  
433 default value of 0.003 to 0.

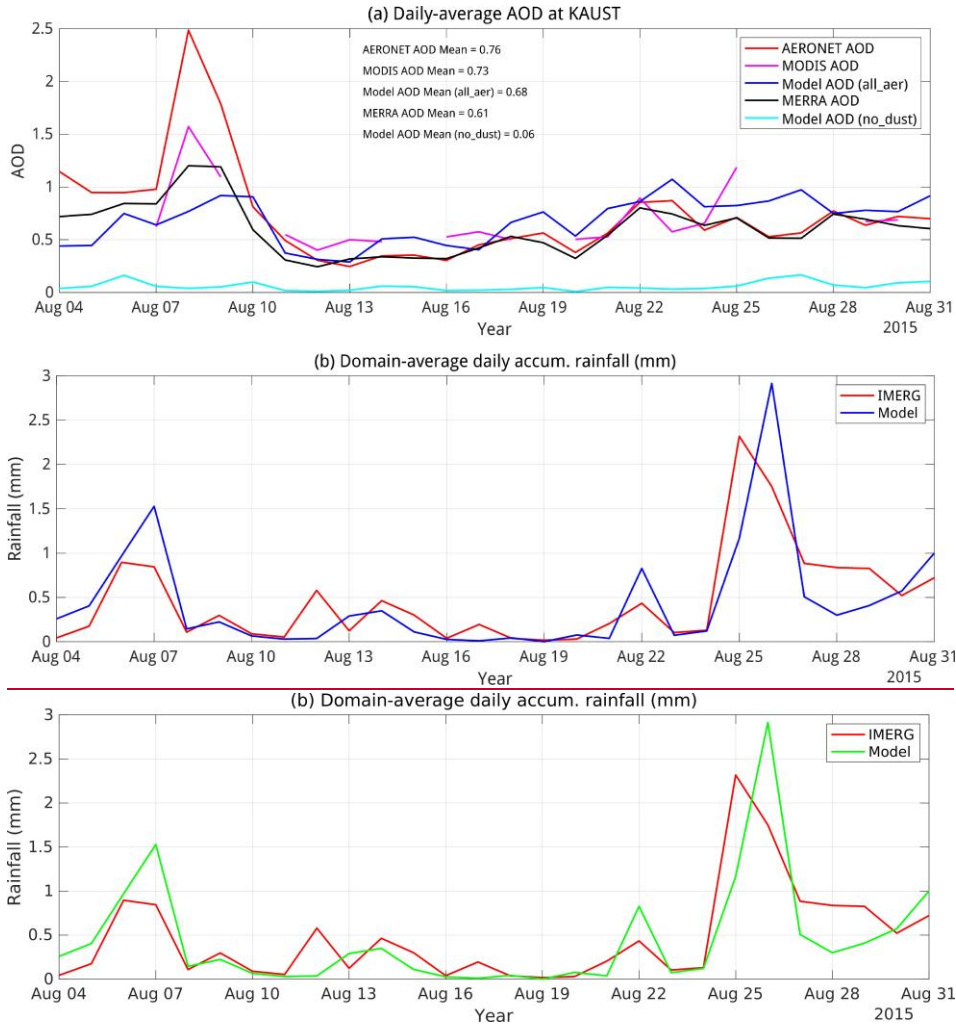
434 The aforementioned effects were calculated for the domain-average daily-accumulated rainfall  
435 over the study period of August 4-31 for each year between 2006–2015 as the difference of  
436 rainfall amounts between the experiments all\_aer (x) and no\_dust (y). The statistical significance  
437 of the effect was determined from the entire 10 years of simulations by creating a uniform  
438 sample of domain-average daily-accumulated rainfall data consisting of 280 (10×28 days) data  
439 points. Statistical analysis were then conducted by separating the data into two categories:  
440 extreme and normal rainfall events. This separation is meaningful because extreme rainfall  
441 events are more influenced by synoptic features whereas normal rainfall events are more  
442 influenced by diurnal-scale sea breeze circulation. High and low rainfall regimes are also known  
443 to respond differently to a given aerosol loading (Li et al., 2011; Choobari, 2018). Extreme  
444 rainfall events were separated from normal rainfall events using the 90<sup>th</sup> percentile value of the  
445 rainfall data from F1 experiment, which was 1.33 mm. Specifically, days with domain-average  
446 daily-accumulated rainfall values greater than or equal to 1.33 mm were considered extreme  
447 rainfall events, whereas those with values below 1.33 mm were considered as normal rainfall  
448 events. With this criterion, the effective numbers of samples (days) available for statistical  
449 analysis were 31 and 243 for extreme and normal rainfall events, respectively. Using MATLAB,  
450 the statistical significance of the effects was determined with the Wilcoxon signed-rank test  
451 (Hollander and Wolfe, 1999; Gibbons and Chakraborti, 2011), which is recommended for data  
452 with non-normal distributions such as rainfall. The null hypothesis of the test considered that the  
453 difference [all\_aer (x) – no\_dust (y)] comes from a distribution with zero median. The same  
454 method was applied to identify significant effects among other parameters including 2-m air  
455 temperature, 10-m winds, and 2-m water vapor mixing ratio.

456 **3. Results**

457 **3.1. Model validation**

458 Here we present a comprehensive evaluation of WRF-Chem from multiple perspectives,  
459 including diurnal cycles, vertical profiles, spatial distribution, and column-averaged properties,  
460 before using the model for answering our research questions listed in section one. All results in  
461 this section correspond to the 'real world' case (all\_aer) unless otherwise stated.





464

465

466 Figure 2. (a) Simulated daily-mean total AOD as compared to MODIS and MERRA-2 data at  
 467 KAUST and (b) simulated daily-accumulated rainfall (mm) as compared to IMERG data,  
 468 averaged over the study domain (d03).

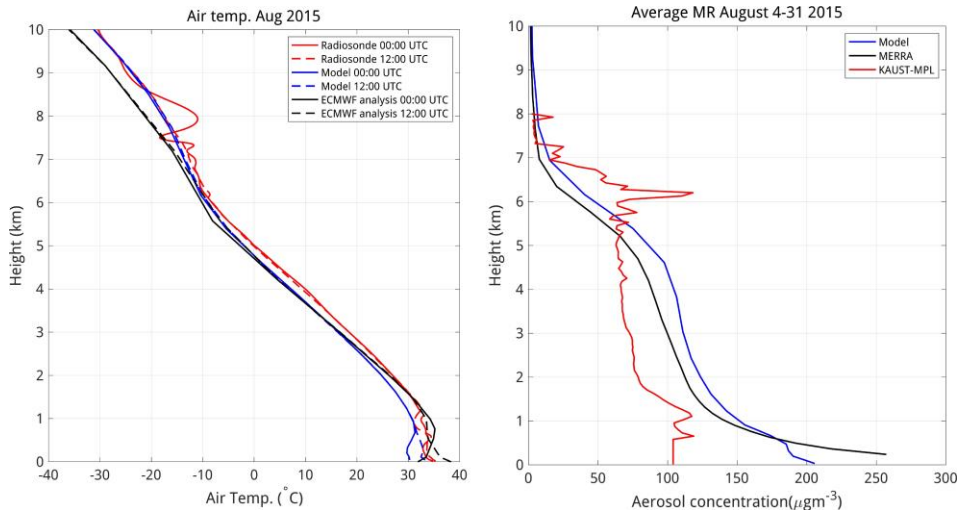
469 Figure 2a shows the domain-averaged (d03) time series of model-simulated AOD (all\_aer case)  
 470 during the study period compared to AERONET, MODIS, and MERRA data. The model AOD  
 471 generally agrees well with both datasets although the peaks during the dust storm (August 8–9)  
 472 tend to be underestimated. The average AOD corresponding to the no\_dust case is also presented  
 473 in Fig. 2a to provide a sense of how much AOD is increased with the addition of dust.



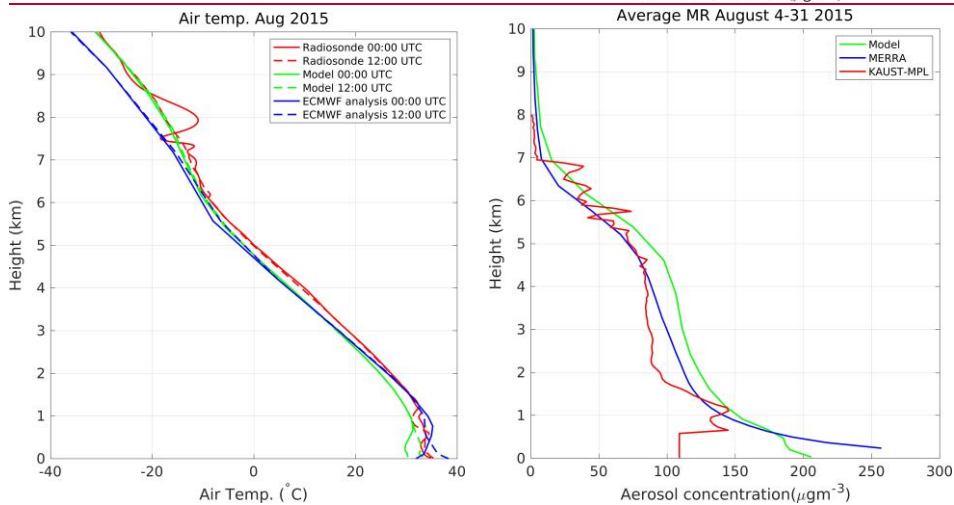
474 The time-series profile of the model-simulated daily-accumulated rainfall follows the trend in the  
475 IMERG data (Fig. 2b). The rainfall peaks including the largest rain event during the study period  
476 (~ Aug 25, 2015) were reproduced reasonably well. Some discrepancy is expected because there  
477 are usually fewer microwave imager observations included in the IMERG data in the  
478 tropical/subtropical region.

479 Fig. S1 illustrates comparison between the simulated aerosol volume size distribution and the  
480 corresponding AERONET size distribution. The two distributions agreed well, especially in the  
481 finer mode that is centered at ~ 0.1 microns, which is critical from the perspective of the  
482 contribution of aerosols in the formation of CCN/IN. It is also important to note that this finer  
483 mode was non-existent in the model when using the default aerosol size distribution. Therefore,  
484 we adjusted both dust emission fractions (Table S1) as well as MOSAIC dust size fractions  
485 (Table S2) so that the resulting size distribution matched the AERONET data more accurately, as  
486 mentioned earlier.

487 Figure 3 shows the model-simulated vertical profiles of air temperature (left) and aerosol  
488 concentrations (right) compared to key observations. The simulated temperature profile was  
489 generally consistent with the radiosonde observations as well as ECMWF operational analysis  
490 with some discrepancies at the cloud-level heights and near the surface. The temperature at the  
491 site does not show large daytime and nighttime variations. Figure 3 also shows the profiles of  
492 aerosol concentrations at KAUST averaged over the study period. The profiles of the model,  
493 MERRA-2, and LIDAR data show some similarity but the model and MERRA-2 generally  
494 overestimate concentration by about 50% compared to LIDAR data. were identical~~The mismatch~~  
495 is greater near the surface. However, the model and MERRA-2 slightly overestimated aerosol  
496 concentrations near the surface compared to the LIDAR data.

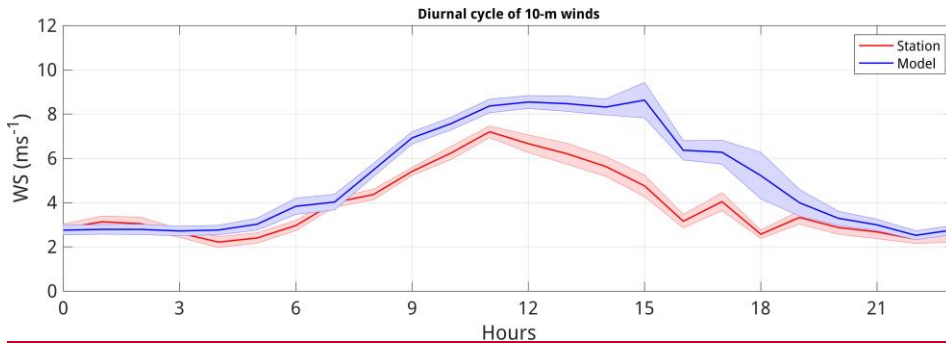


497

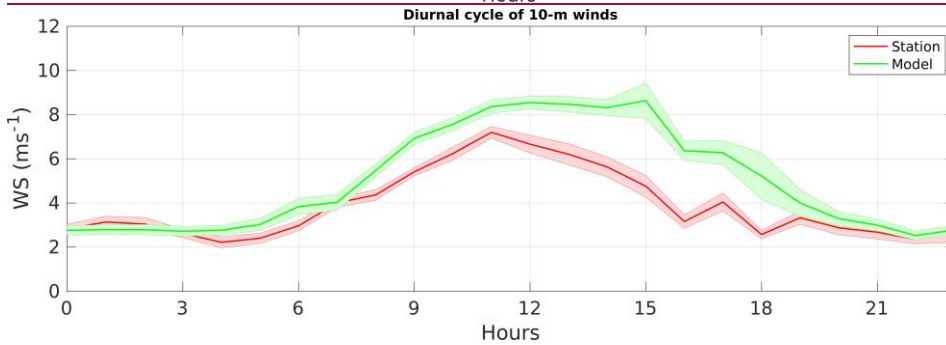


498

499 Figure 3. Average vertical profiles of air temperature (left) and aerosol concentrations (right)  
 500 compared to reference observations. The air temperature profile was compared against ECMWF  
 501 operational analysis and radiosonde station data at King Abdul Aziz International Airport,  
 502 Jeddah (21.7N, 39.18E) during the daytime (12:00 UTC) and nighttime (00:00 UTC) by  
 503 averaging during the study period (4–31 August 2015). Simulated aerosol mixing ratios were  
 504 compared against MERRA-2 reanalysis and MPL LIDAR station data at KAUST (22.30N,  
 505 39.10E) for 4–31 Aug 2015.



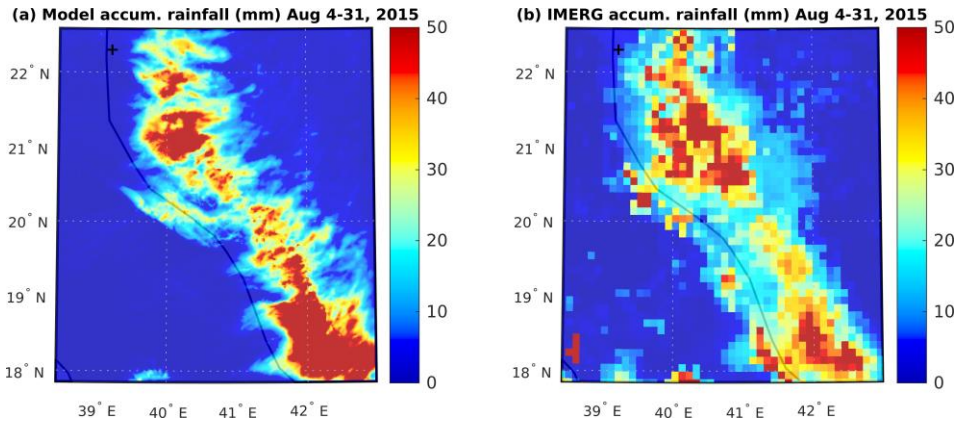
506



507

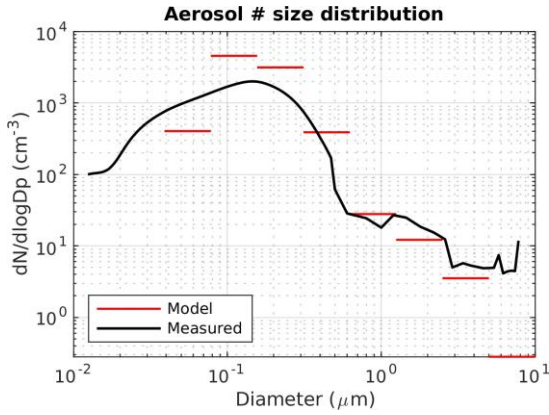
508 Figure 4. Diurnal profile of the model-simulated wind speeds compared to station data over the  
 509 study period (Aug 4–31, 2015) at KAUST (22.30N, 39.10E). The shading represents the standard  
 510 error of the mean calculated from the hourly wind speeds.

511 Figure 4 shows the wind speed diurnal profile in the model and the observations at KAUST  
 512 during the study period (Aug 4-31, 2015), which were reasonably consistent. The model  
 513 overestimated wind speeds mainly during the afternoon, which is when the flow is more chaotic  
 514 as the sea breezes meet the northeasterly harmattan winds. The peak winds occur at ~ 12:00 UTC  
 515 (15:00 local time), which correspond to the sea breeze maxima. The root mean squared error  
 516 (RMSE) of the simulated wind speed is  $1.18 \text{ m s}^{-1}$ , which is 29.6% of the observed mean. This  
 517 level of discrepancy is reasonable since anemometers also typically have uncertainty up to  $\pm 0.5$   
 518  $\text{m s}^{-1}$ .



519  
 520 Figure 5. Spatial distribution of accumulated rainfall (Aug 4–31, 2015) (a) model (b) IMERG  
 521 data. The location of KAUST is marked by a plus sign.

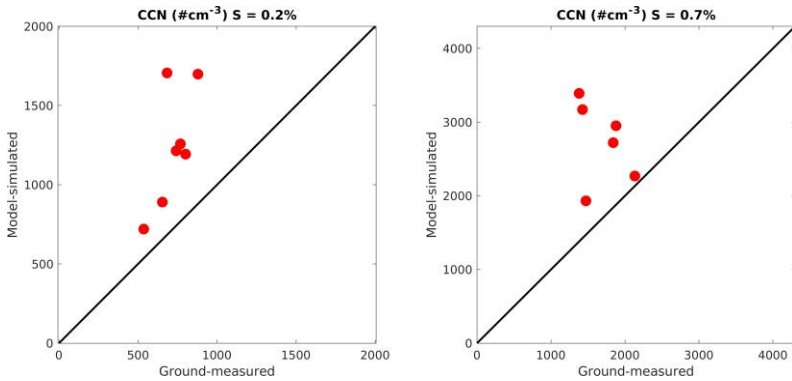
522 Figure 5 shows the spatial distribution of accumulated rainfall during the study period over the  
 523 study domain (d03) compared to the IMERG data, both of which were reasonably consistent  
 524 with each other. The rainfall pattern follows the length of the Sarawat Mountains stretching north  
 525 to south. As the model shows, larger amounts of rainfall occurs in the areas with higher  
 526 mountains. In the inland areas away from coast, rainfall distribution is also determined by  
 527 synoptic rain events. For example, during the period of comparison, there were two events  
 528 (August 7 and August 26) categorized as extreme rainfall events. This could be the reason why  
 529 the IMERG data shows stronger rainfall in the north than in the south. The model has larger  
 530 rainfall bias during such extreme rain events (Fig 2b) so the spatial distribution appear somewhat  
 531 inconsistent with the IMERG data. However, note that IMERG data also show high RMSE (up  
 532 to 30 mm) in this region compared to rain gauge measurements (Mahmoud et al., 2018).The  
 533 rainfall pattern follows the length of the Sarawat Mountains stretching north to south. The  
 534 southern areas of the domain receive more rainfall due to the presence of higher mountains.



535

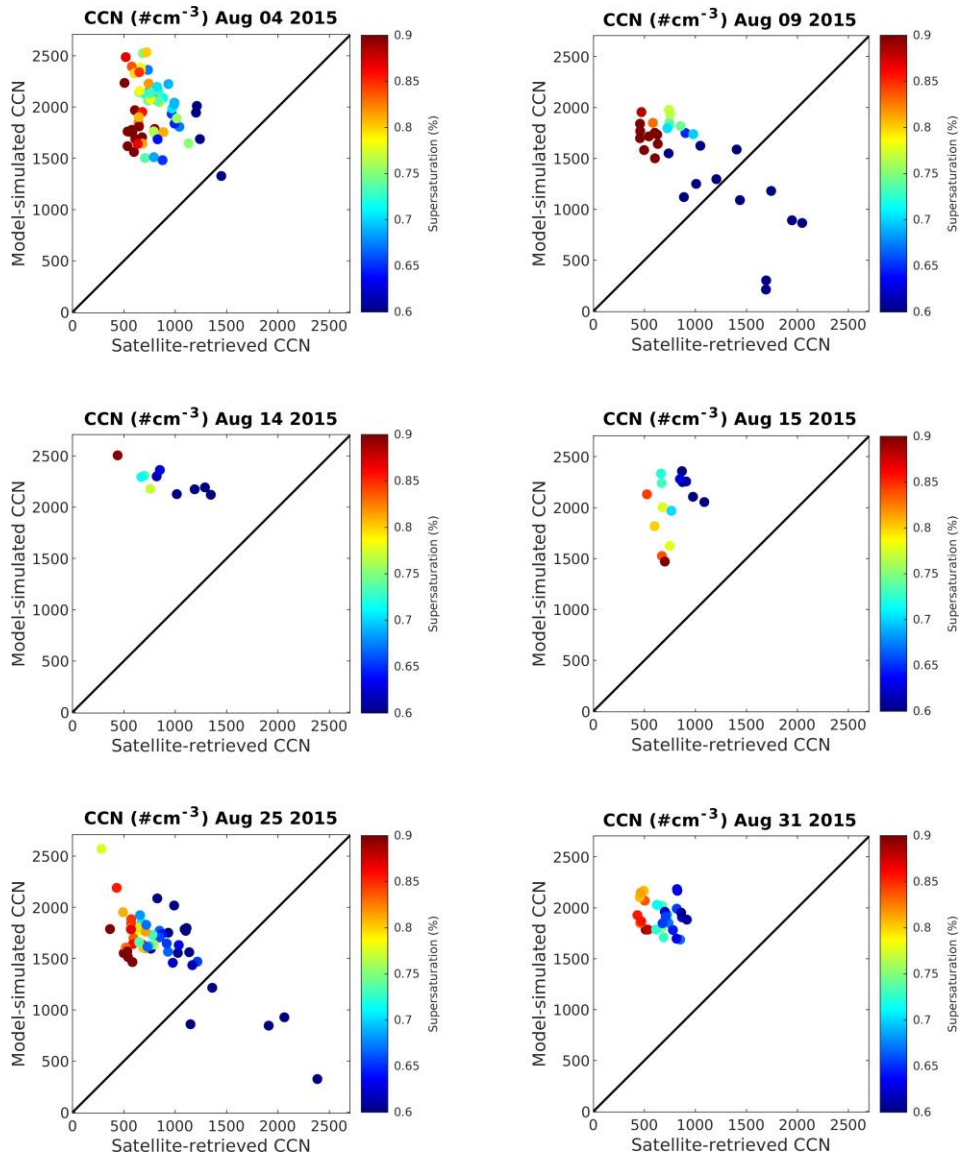
536 Figure 6. Comparison of model-simulated aerosol number concentrations ( $\text{cm}^{-3}$ ) corresponding  
 537 to MOSAIC size bins compared to flight measured values during the field campaign of August  
 538 2009. The widths of the red lines represent the widths of the eight MOSAIC bins. The model  
 539 data (8-bins) were extracted at the exact latitude, longitude, and altitude corresponding to the  
 540 flight data by 3d linear interpolation and averaged over the days available (Aug 11–30, 2009)  
 541 during the time of measurements (~06:00 to 09:00 UTC).

542 Figure 6 shows the aerosol number size distributions compared to the flight data, ~~which are~~  
 543 reasonably similar. Results indicate that 8-bin MOSAIC sectional aerosol scheme can represent  
 544 the atmospheric aerosol size distribution well. The peak number concentration occurs at  $\sim 0.15$   
 545  $\mu\text{m}$  diameter in both model and flight data. Although the size distribution patterns appear similar  
 546 in model and observation, the differences in number concentrations are high particularly at 0.06-  
 547 0.2  $\mu\text{m}$  (note the logarithmic scale).



548

549 Figure 7. Comparison between model-simulated CCN number concentrations and ground-  
550 measured values at the PME station (18.24N, 42.46E) at supersaturations of 0.2 and 0.7%. The  
551 CCN number concentrations correspond to the ground station at Abha. The plotted point  
552 represents the average value for different days of measurement from August 11–30, 2009  
553 approximately from 02:00 to 08:00 UTC.



554

555 Figure 8. Model-simulated vs. VIIRS satellite-retrieved CCN number concentrations for six days  
 556 of available data within the study domain during the August 2015 study period. The data points  
 557 represent CCN number concentrations at the cloud base of existing convective cells on different  
 558 days over the study domain (d03).

559 Figure 7 shows the comparison between the CCN number concentrations obtained from the  
560 model and from ground station at two super-saturations measured during the Aug 2009 field  
561 campaign. CCN number concentrations are generally overestimated by the model at both  
562 low/high super-saturations by up to a factor of two.

563 Figure 8 shows the comparison between the model-simulated CCN number concentration and the  
564 satellite-retrieved data from VIIRS. Similar to the previous comparison, the model overestimates  
565 CCN number concentration compared to the VIIRS data also by approximately a factor of two.  
566 ~~This order of difference, although large, is reasonable for microphysical parameters given the~~  
567 ~~high uncertainty in their parameterization.~~

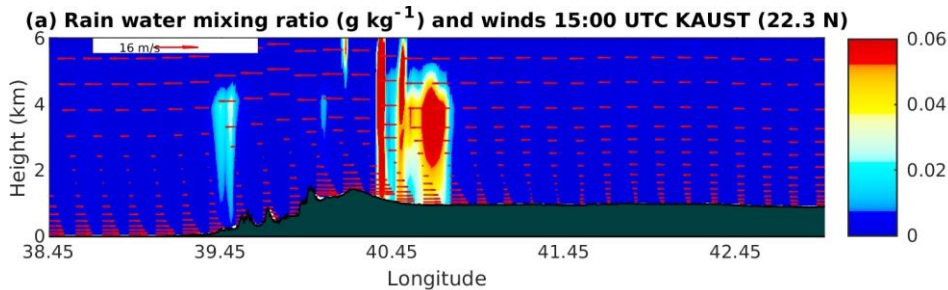
568 Since the rainfall amount is reasonably well simulated (Figs 2b and 5), the overestimation of  
569 CCN concentration suggests that CCN is not a limiting factor for rain formation in the study  
570 region. These findings are reasonable because the study region is not aerosol-limited, and  
571 therefore cloud growth and rainfall do not strongly depend on the changes in CCN  
572 concentrations, unlike in other aerosol-limited areas (Koren et al., 2014).

### 573 3.2. Rainfall diagnostics

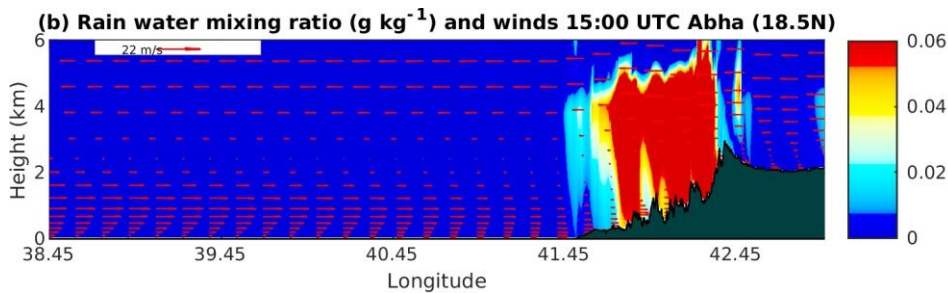
574 This section presents the diagnostic results of the key parameters related to the rainfall process to  
575 demonstrate the accuracy of our rainfall calculations.

576 Figures 9a and 9b show the rainwater mixing ratio in two longitudinal cross-sections, one  
577 passing through KAUST (22.3N, 39.10E), a relatively dry area, and another through Abha  
578 (18.25N, 42.51E), a region known for rainfall abundance. Maximum rainfall occurs in the  
579 evening at 15:00 UTC (6 pm local time) at both locations in the convergence boundary (i.e.,  
580 where the sea breezes meet with Harmattan winds). The rainfall is limited to a ~6 km height  
581 around the hilly terrain. There is less rainfall near the coast, where the majority of the population  
582 resides, because the rain evaporates well before it reaches the ground due to high surface  
583 temperature. The moisture-laden sea breezes can be prominently seen during the day within ~1.5  
584 km height. Furthermore, these sea breezes strengthen as they travel upslope over the Sarawat  
585 Mountains (black shades). The dry northeasterly Harmattan winds, which usually bring dust  
586 from the desert towards the Red Sea during dust storms (Prakash et al., 2014; Parajuli et al.,  
587 2020) can be seen at a ~3–6 km height.





588



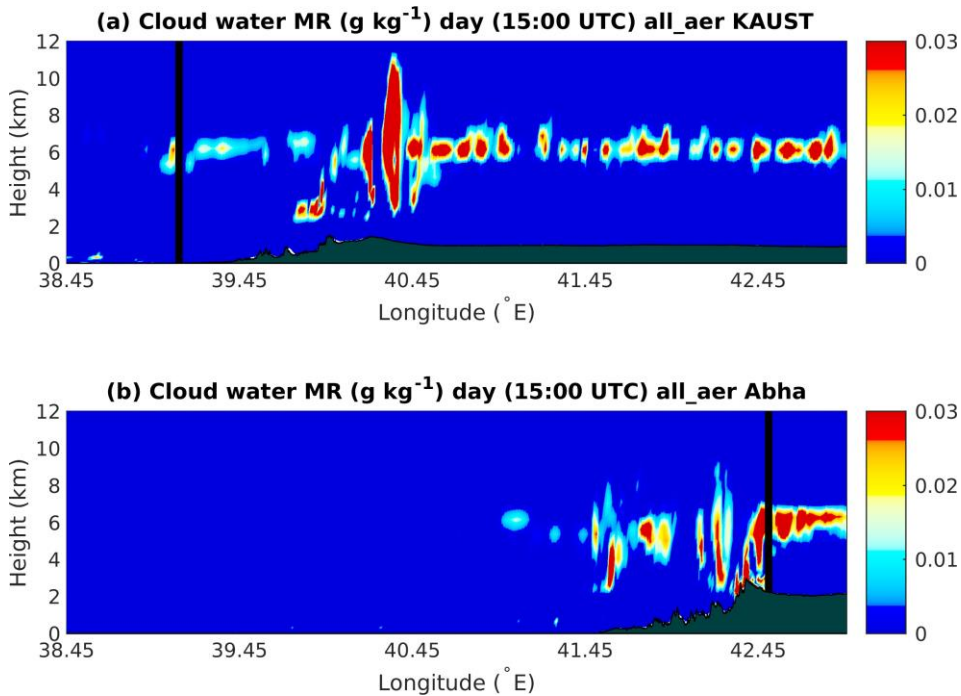
589

590 Figure 9. Rainwater mixing ratio and wind vectors averaged at ~~the time of rainfall maxima~~ 15:00  
 591 UTC over the study period (August 4–31, 2015) at two longitudinal cross-sections passing  
 592 through (a) KAUST and (b) Abha.

593 Figure 10 shows the cloud water mixing ratio profiles at the longitudinal profiles passing through  
 594 KAUST and Abha at rainfall maxima (15:00 UTC), which provides insights into the vertical  
 595 position and extents of the clouds. Most clouds are observed at a ~5–6 km height at both  
 596 locations, suggesting that the warm cloud processes are responsible for causing rainfall in the  
 597 region. The height of deeper, convective clouds ranges from ~3 to 10 km. The clouds are  
 598 generally deeper where rainfall is more intense, which suggests the existence of local convective  
 599 activity. The horizontal location of clouds are consistent with the locations of rainfall maxima in  
 600 Fig. 9.

601 Although more clouds are observed over KAUST (Fig. 10a) than over the Abha region (Fig.  
 602 10b), more rainfall occurs over Abha because the steeper topographic slope over the Abha region  
 603 facilitates stronger orographic lifting of the moist air mass, which converts more easily into rain.  
 604 The temperature over the Abha region is cooler than that over KAUST region, consequently the  
 605 sea breezes over the Abha region are weaker than at KAUST (Figure 9). Thus, the maximum  
 606 rainfall occurs in the front (lee) side of the mountains in Abha (KAUST) region. Additionally,  
 607 there is more evaporation over the KAUST region due to its higher surface temperature  
 608 compared to the Abha region, which reduces the amount of rainfall that reaches the ground but  
 609 contributes to more cloud formation.

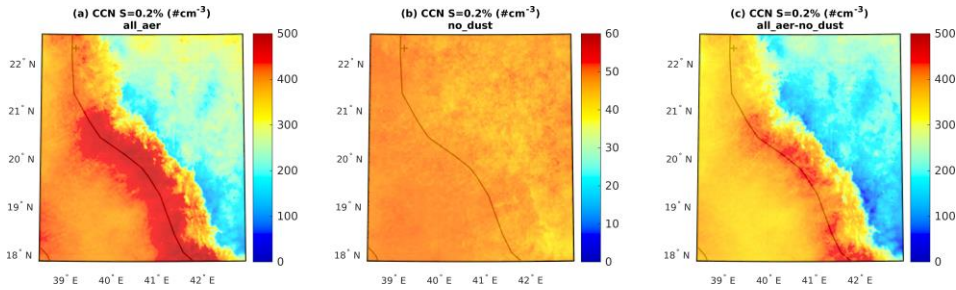
610



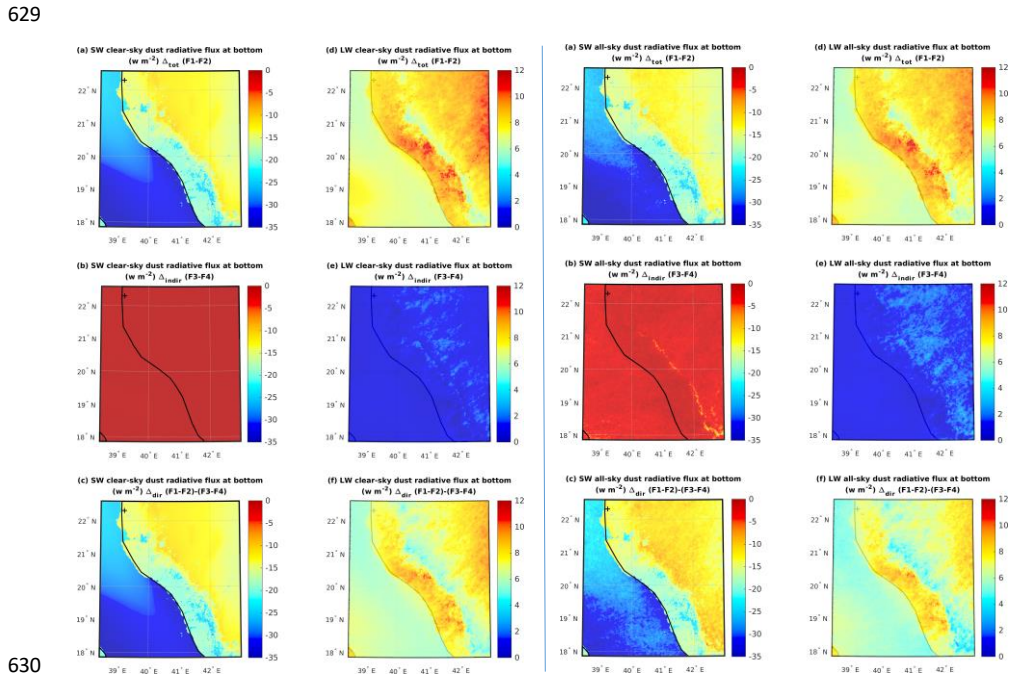
611

612 Figure 10. Profile of cloud water mixing ratio for a longitudinal section passing through (a)  
 613 KAUST and (b) Abha, averaged for August 4–31, 2015 at 15:00 UTC. The location of KAUST  
 614 and Abha City are indicated with black vertical lines.

615 Figure 11 shows the spatial distribution of the CCN number concentrations at a 0.2%  
 616 supersaturation for all\_aer (F1), nodust (F2) and their difference (F1-F2). In the absence of dust,  
 617 CCN # concentrations are generally uniform throughout the domain (Fig. 11b). There is up to  
 618 ten-fold increase of CCN after addition of dust (Fig. 11a), making dust the major contributor of  
 619 total CCN. The simulated CCN # concentrations in no\_dust case are in the range of ~40–50 (Fig.  
 620 11b), which are too low compared to the observed CCN # concentrations, which are roughly in  
 621 the range of 500–1000 in observations (Figs. 7 and 8). Although model CCN # concentrations  
 622 are overestimated compared to observations as discussed previously, it is clear that addition of  
 623 dust brings the CCN # concentrations much closer to observations (Fig. 11a) compared to the  
 624 case without dust (Fig. 11b).



625  
 626 Figure 11. CCN number concentrations at 0.2% supersaturation at a cloud-level height (570 hPa)  
 627 averaged at 15:00 UTC for August 4–31, 2015 (a) all\_aer (F1), no\_dust (F2), and (c) the  
 628 difference F1-F2.



630  
 631 Figure 12. Effects of dust on the clear-sky (left two columns) and all-sky (right two columns)  
 632 radiative fluxes at the bottom of the atmosphere calculated from 10-year August average WRF-  
 633 Chem simulations.

634 To accurately evaluate the effect of dust on rainfall, it is important to ensure that the dust effects  
 635 on radiative fluxes are reasonably well simulated. To gain insights into the relative importance of

636 dust and clouds on radiative budget, the effects of dust on radiative fluxes for clear-sky (without  
637 clouds) and all-sky (with clouds) conditions were calculated separately.

638 Figure 12 (left two columns) shows the effect of dust on clear-sky radiative flux in terms of total,  
639 indirect, and direct effects at the bottom of the atmosphere. Dust decreases the radiative flux that  
640 reaches the surface due to SW scattering and absorption, and therefore the direct effect is  
641 negative, which in turn governs the total effect. The effect of dust on LW radiative flux is  
642 positive because dust absorbs LW radiation. The clear-sky indirect effects are non-zero but very  
643 small compared to the direct effects. These small indirect effects arise due to feedback processes  
644 that cause small perturbations in cloud properties. Figure 12 (right two columns) shows the  
645 effects of dust on all-sky (i.e., with clouds) radiative flux. The all-sky radiative fluxes exhibited  
646 small changes in the indirect and direct effects due to the clouds both in the SW and LW bands.  
647 The magnitude and sign of change in SW and LW dust radiative fluxes are consistent with the  
648 results of Klingmüller et al., 2019.

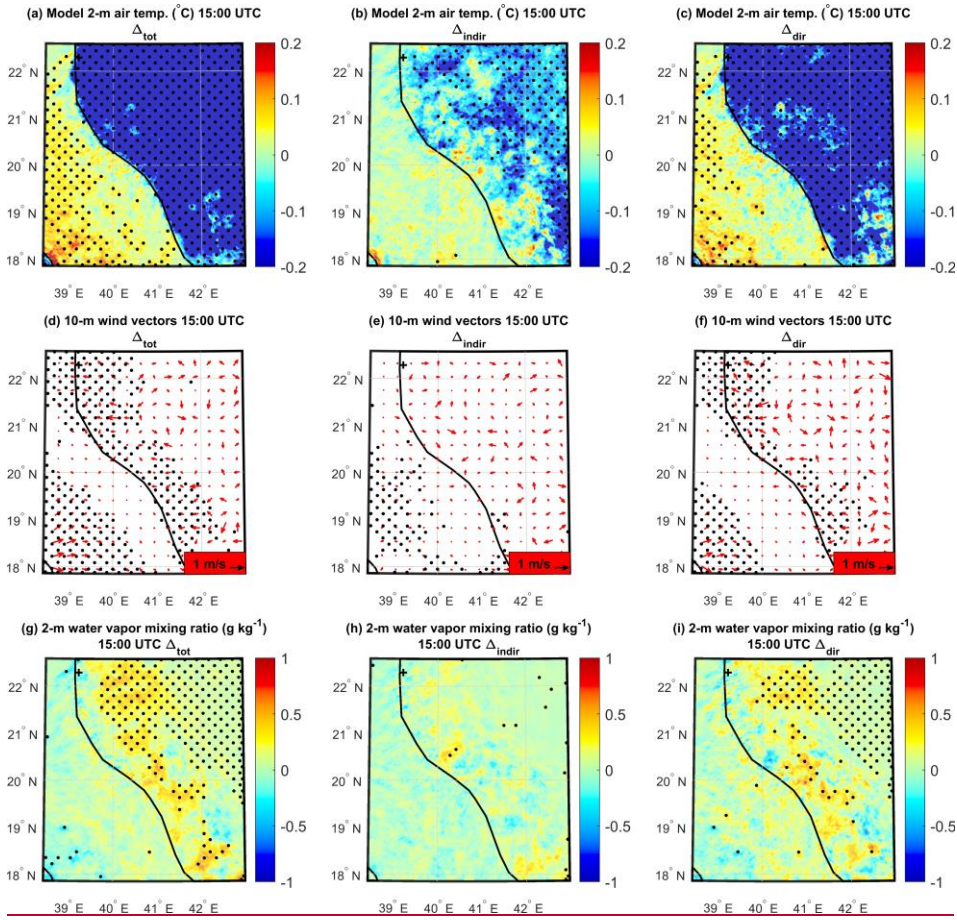
### 649 **3.3. Dust effect on rainfall**

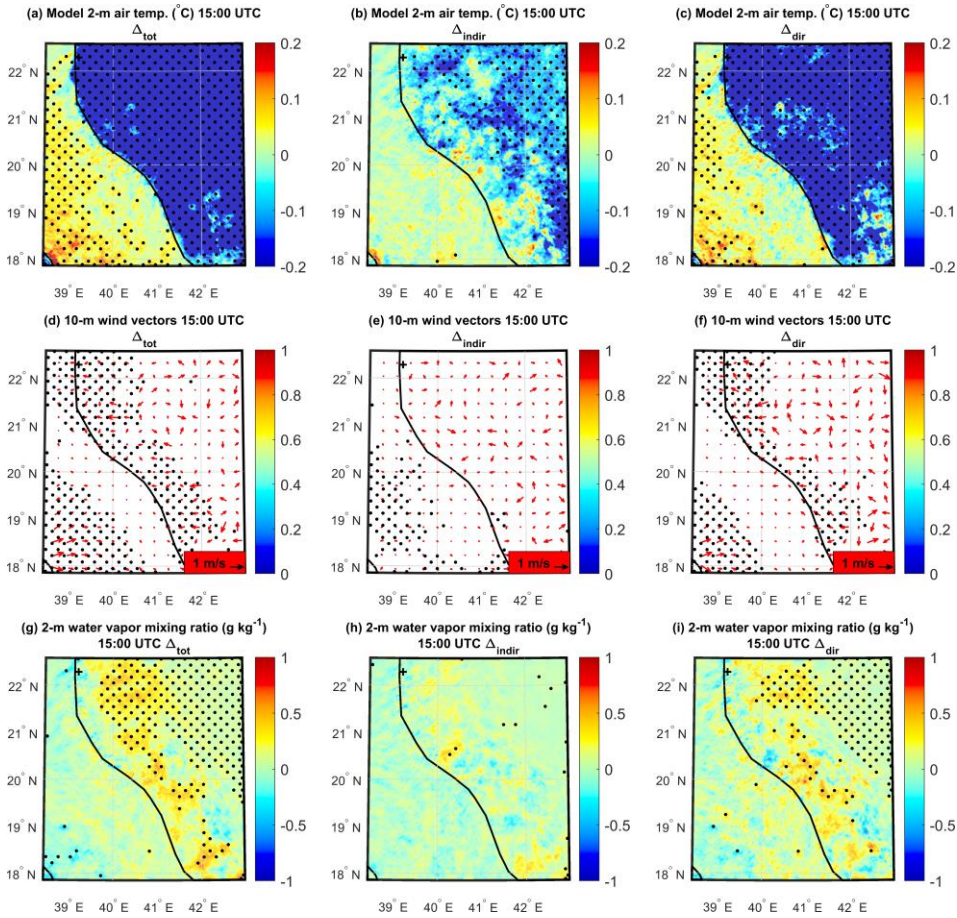
#### 650 **3.3.1. Dust direct and indirect effects**

651 Figure 13 (a, b, c) shows the dust effects on 2-m air temperature. Dust induces a total cooling  
652 effect over the lands (Fig. 13a), which appear to be dominated by the direct effects (Fig.13c)  
653 rather than the indirect effects (Fig. 13b). Dust also induces warming in some inland areas and  
654 over the ocean, which is affected by both the indirect and the direct effects (Figs. 13b and 13c).  
655 The total and direct effects were largely statistically significant (black dots) but the indirect  
656 effects were significant only over the lands.

657 In turn, the cooling and warming of the land surface affects the winds. Figures 13 (d, e, f) shows  
658 the effects of dust on surface winds. As with surface temperature, the direct effects had a  
659 stronger influence compared to the indirect effects on winds as well. The direct effects on winds  
660 were statistically significant along the coast, which confirms the impact of dust's direct effects  
661 on sea breezes.

662 A high positive moisture anomaly was observed over the land (Fig. 13 g, h, i), particularly with  
663 the direct effect (Fig. 13i). The moisture increase over the land caused by the direct effect is  
664 further amplified by the weaker indirect effect making the total effect more widespread. The  
665 increased moisture due to the direct and total effect were both statistically significant. The reason  
666 for the positive moisture anomaly over the land in relation to sea breeze is explained in the  
667 section below.





669  
 670 Figure 13. Spatial patterns of the  $\Delta_{tot}$  (F1-F2),  $\Delta_{indir}$  (F3-F4), and  $\Delta_{dir}$   $\{(F1-F2)-(F3-F4)\}$  for 2-m  
 671 air temperature (a, b, c), 10-m winds (d, e, f) and 2-m water vapor mixing ratio (g, h, i) averaged  
 672 at the time of rainfall maxima (15:00 UTC) over the entire study period (August 2006–2015).  
 673 Black dots represent areas where the effect is statistically significant at 95% confidence interval.

674 Table 3. Total, indirect, and direct effects of dust on rainfall for extreme and normal rainfall  
 675 events.

Case	Total effect ( $\Delta_{tot}$ )			Indirect effect ( $\Delta_{indir}$ )			Direct effect ( $\Delta_{dir}$ )		
	Domain average rainfall (mm) F1 all_aer	Domain average rainfall (mm) F2 no_dust	Effect (F1-F2) mm (%)*	Domain average rainfall (mm) F3 all_aer	Domain average rainfall (mm) F4 no_dust	Effect (F3-F4) mm (%)*	all_aer	no_dust	Effect (F1-F2) - (F3-F4) mm (%)*
<b>Extreme rainfall events</b>	2.404	2.264	0.140 (6.05)	2.347	2.242	0.105 (4.54)	0.057	0.022	0.035 (1.51)
	Significant? (p-value)		yes (0.004)	Significant? (p-value)		yes (0.048)	Significant? (p-value)		no (0.367)
<b>Normal rainfall events</b>	0.287	0.290	-0.003 (-1.02)	0.306	0.292	0.014 (4.76)	-0.019	-0.002	-0.017 (-5.78)
	Significant? (p-value)		no (0.083)	Significant? (p-value)		yes (<0.0001)	Significant? (p-value)		yes (<0.0001)

676 \*Percentage of average rainfall (F1, F2, F3, and F4).

677 Table 3 summarizes the effects of dust on rainfall for extreme and normal rainfall events  
 678 calculated in terms of a 10-year average daily-accumulated rainfall over the study domain (d03)  
 679 during the month of August. For the extreme-rainfall events, the total effect (0.140 mm), indirect  
 680 effect (0.105 mm), and direct effect (0.035 mm) were all positive (enhancement). The total,  
 681 indirect, and direct effects in terms of percentage of average rainfall are 6.05, 4.54, and 1.51%,  
 682 respectively. The total and indirect effects are significant at the assumed 5% significance level  
 683 but not the direct effect. The direct effect, although small and statistically insignificant,  
 684 contributed to the larger indirect effect making the total effect statistically significant.

685 For the normal-rainfall events, the change in rainfall amount due to total, indirect, and direct  
 686 effects are -0.003, 0.014, and -0.017 mm, respectively. Both the rainfall changes from the  
 687 indirect effect (positive) and the direct effect (negative) were statistically significant at the  
 688 assumed 5% significance level. The total, indirect, and direct effects in terms of percentage of  
 689 average rainfall were -1.02, 4.76, and -5.78%, respectively. The indirect and direct effects, which  
 690 are opposite in sign and nearly equal in magnitude, cancel each other out making the total effect  
 691 small and statistically insignificant. However, note that the total effect could be considered  
 692 significant if the significance level was increased to 10% ( $p = 0.083$ ).

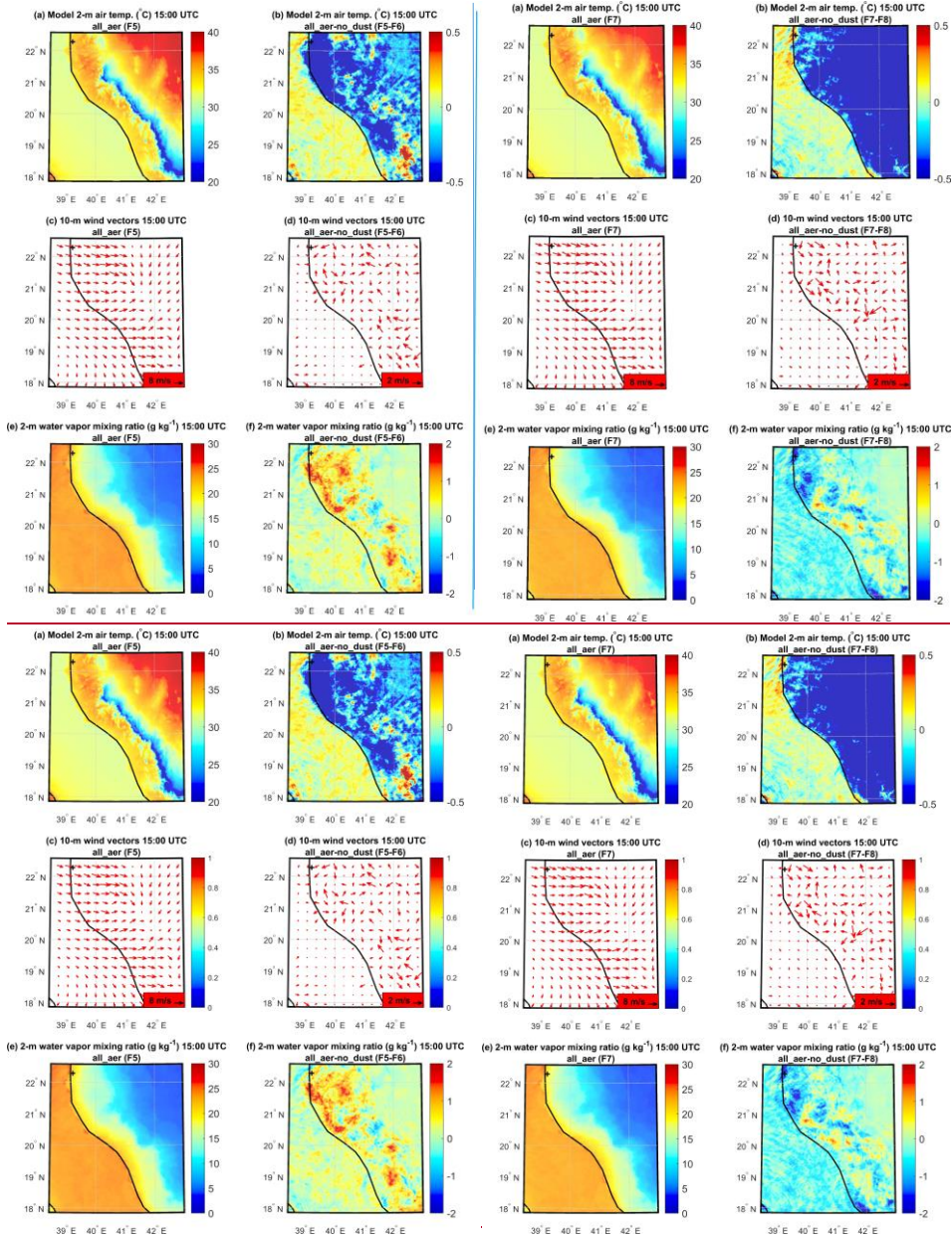
693 Although the domain-average rainfall change caused by dust averaged over multiple years  
 694 (2006–2015) appeared small, the effect can be large at different ~~grid points~~ locations and times.  
 695 For example, for the year 2015, the accumulated rainfall changes (total effect) for August at the  
 696 grid point maxima and minima within the domain were 92.0 mm (190.0%) and -70.0 mm (-  
 697 46.6%), respectively.

698 The total, indirect, and direct effects were also calculated for the total number of wet days  
 699 (average daily-accumulated rainfall  $\geq 1$  mm). The number of wet days increased by three due to

700 the indirect effects but decreased by four by the direct effects, resulting in a total net increase of  
701 one day.

702 Table 3 summarizes the dust direct effect ( $\Delta_{\text{dir}}$ ) calculated using the standard method mentioned  
703 in section 2.3.2 [i.e., by subtracting the indirect effect ( $\Delta_{\text{indir}}$ ) from the total effect ( $\Delta_{\text{tot}}$ )]. To  
704 verify the validity of this method, we compared the results obtained from this method with the  
705 direct effect calculated from direct-effects-only experiments (F5, F6, Table 2) for Aug 2015. The  
706 direct-effects-only experiments allow us to more directly calculate effects of dust on rainfall  
707 induced by land surface cooling or warming using the same model but with simpler settings  
708 without the indirect effects. The dust direct effect calculated from these direct-effects-only  
709 simulations (-0.046 mm) agreed very well with the results obtained from the standard method (-  
710 0.045 mm). The consistency of these two results confirms the robustness of our results.





712

713

714 Figure 14. Left two columns: spatial patterns of 2-m air temperature (a, b), 10-m wind vectors (c,  
715 d), and 2-m water vapor mixing ratio (e, f) averaged at the time of sea breeze maxima (15:00  
716 UTC) throughout the period of August 4–31, 2015 from the direct-effects-only experiment for  
717 all\_aer case: F5 (first column) and the difference all\_aer-no\_dust: F5-F6 (second column). Right  
718 two columns: same as the left panel but without shortwave absorption, showing all\_aer case (F7)  
719 and the difference all\_aer-no\_dust (F7-F8).

720 The results of the direct-effects-only simulations (F5, F6, Table 2) are presented in Fig. 14 (left  
721 two columns). The cooling effect was dominant in the coastal areas, whereas warming was also  
722 observed in some inland areas particularly in the southern region (Fig. 14b). Figure 14d  
723 demonstrates that the breezes are weakening and even reversing from land to sea in the areas of  
724 cooling (~ 22N) due to the dust direct effects. However, in the areas that exhibited warming  
725 (~18.5N), sea breezes strengthened as the land warming further increased the land-sea thermal  
726 contrast.

727 A strong positive moisture anomaly was observed over the land in the direct-effects-only  
728 simulations (Fig. 14f, left two columns). This is intriguing because we expected a reduction in  
729 moisture transport over the land due to the dust direct effects as a result of land surface cooling,  
730 and a subsequent weakening of the sea breezes (Mostamandi et al., 2021). Figure 14 also shows  
731 the results of the additional experiments in which the SW absorption was restricted (F7, F8), as  
732 mentioned in section 2.3.2. Given that the SW absorption was eliminated, this experiment allows  
733 us to better understand the effect of dust on sea breezes via the cooling effect alone (i.e., without  
734 warming effects). However, note that the effect of dust is complex as it warms the atmosphere  
735 and cools the surface (Choobari et al., 2014). Nevertheless, this elimination of SW absorption  
736 removed the dust-induced warming observed earlier over the land (compare Figs. 14b left and  
737 right panel). Since the cooling effect becomes dominant, sea breezes are now weaker and  
738 therefore the landward moisture transport is considerably reduced, which is evident by  
739 comparing the left and right panel of Figs. 15f. These results confirm that the high positive  
740 moisture anomaly over the land by dust direct effects is caused by the strengthening of sea  
741 breezes as a result of dust-induced warming. Although it is generally understood that SW  
742 absorption decreases the radiation reaching the surface and thus cools the surface (e.g., Choobari  
743 et al., 2014), we observed surface warming because most of the atmospheric dust here lie very  
744 near to the surface (Parajuli et al., 2020), which is evident in Fig. 3b. The observed effects on  
745 breezes are broadly consistent with those of Mostamandi et al. (2021), who also observed a  
746 weakening of albedo-induced land cooling on sea breezes associated with the strong land  
747 cooling, which reduces the thermal contrast between the land and the ocean.

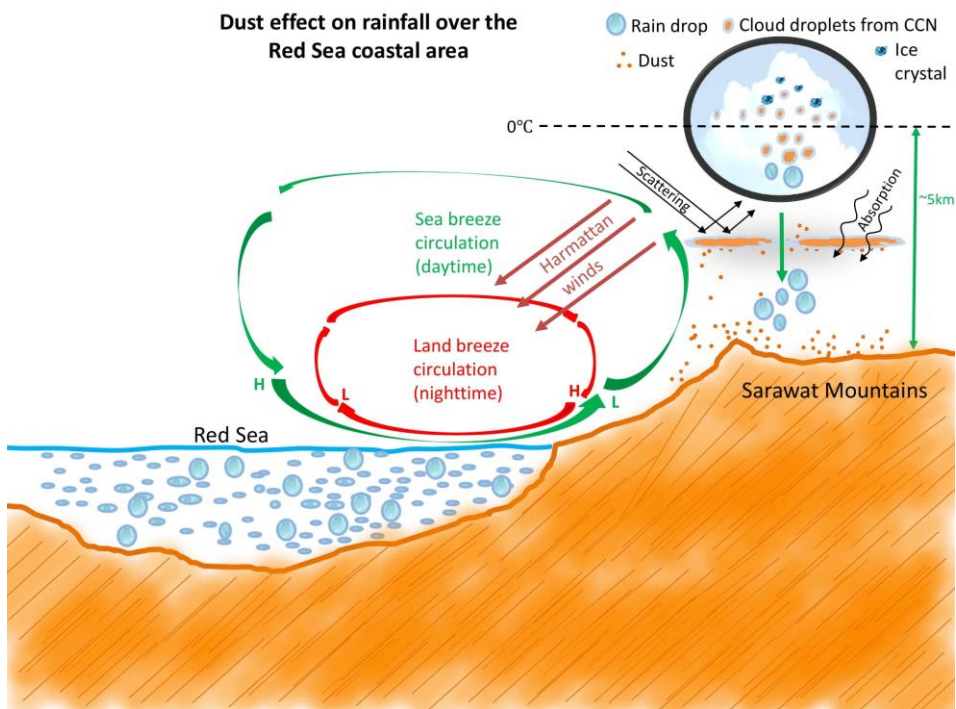
#### 748 4. Summary discussion and limitations

749 The rainfall over the Red Sea coastal area has a strong diurnal cycle peaking at approximately  
750 15:00 UTC coinciding with the moisture-laden westerly sea breezes uplifted by the coastal  
751 topography meeting the easterly Harmattan winds over the Sarawat Mountains. The dust  
752 modifies rainfall through both indirect and direct effects over the study region. In summary, dust  
753 enhances rainfall for extreme rainfall events but suppresses rainfall for normal rainfall events.

754 These results are consistent with previous studies (e.g., Choobari, 2018; Li et al., 2011), which  
 755 show that dust increases (decreases) rainfall in high (low) rainfall conditions. Since the  
 756 calculated indirect effects are small, our results are also consistent with that of Koren et al.  
 757 (2014), which also showed the indirect effects on warm clouds is less sensitive to aerosol loading  
 758 over polluted atmosphere than over clean atmosphere.

759 by affecting the sea breeze circulation. The various pathways of dust-rainfall interactions  
 760 occurring over the Red Sea coast are summarized in a schematic diagram presented in Fig. 15.

Formatted: Font color: Auto



761  
 762 Figure 15. Schematic diagram representing the rainfall processes and dust-rainfall interactions  
 763 over the Red Sea coast.

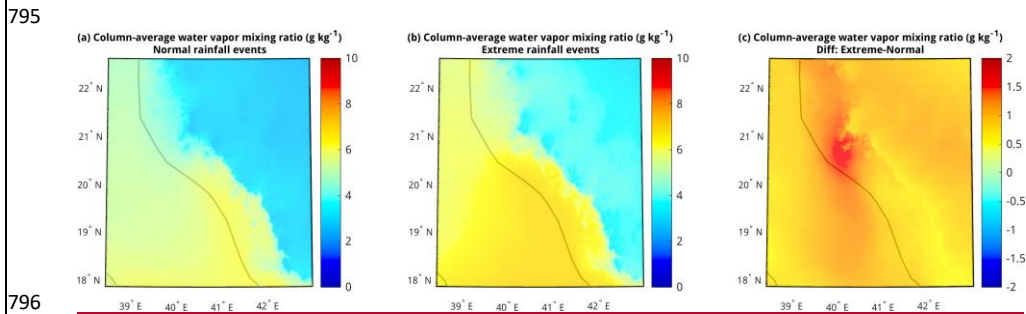
764 In summary, dust enhances rainfall for extreme rainfall events but suppresses rainfall for normal  
 765 rainfall events. These results are consistent with previous studies (e.g., Choobari, 2018; Li et al.,  
 766 2011), which show that dust increases (decreases) rainfall in high (low) rainfall conditions. by  
 767 affecting the sea breeze circulation. The various pathways of dust-rainfall interactions occurring  
 768 over the Red Sea coast are summarized in a schematic diagram presented in Fig. 15.

769 For normal rainfall events, the suppressing direct effect dust effect on rainfall mainly occurs  
 770 through both direct and indirect effects, which is are strong and statistically significant, which is  
 771 governed by the weakening of the diurnal scale sea breezes in response to SW cooling by dust.

Formatted: Font color: Auto

772 As Table 3 shows, the negative dust direct effect (-5.78%) is slightly stronger than the positive  
773 indirect effect (+4.76%) for the normal rainfall events. For these events, the dust direct effect is  
774 caused by the weakening of sea breeze circulation in response to SW cooling by dust as  
775 explained previously. The various pathways of dust-rainfall interactions occurring over the Red  
776 Sea coast are summarized in a schematic diagram presented in Fig. 15.

777 -For extreme rainfall events, the direct effect was positive but was not statistically significant,  
778 which could perhaps become significant with a larger sample size. For these rainfall events, the  
779 dust effect occurs through a different physical mechanism governed by the indirect effects. As  
780 Table 3 shows, the indirect effect (+4.54%) is stronger than the direct effect (+1.51%). The  
781 reason why indirect effect is stronger than the direct effect for extreme rainfall events is that,  
782 extreme rain events are caused by larger synoptic processes, and during their occurrence, the  
783 local-scale breeze effect becomes comparatively weaker. Consequently, the indirect effect  
784 becomes dominant compared to the direct effect. Whether the indirect effect is positive or  
785 negative is mainly determined by prevailing dust concentration and water vapor availability.  
786 During the extreme rainfall events, the water vapor is abundantly available so water vapor is not  
787 a limiting factor for rain formation. Since CCN # concentrations are abundant (Figs. 7, 8), dust  
788 concentration is not a limiting factor in this desert study domain either. In such high dust  
789 concentration and abundant water vapor scenario, rain droplets keep growing (Chooari, 2018;  
790 Li et al., 2011) rendering the indirect effect to be positive. To demonstrate this mechanism  
791 further, we plotted the column-average water vapor mixing ratio for normal rainfall events and  
792 extreme rainfall events separately (Fig. 16). It is clear that the average water vapor concentration  
793 is remarkably higher in extreme rainfall events compared to normal rainfall events (note the  
794 positive difference in Fig. 16c), which supports the above explanation.



797 Figure 16. Column-average water vapor mixing ratio for (a) normal rainfall events (b) extreme  
798 rainfall events and (c) the difference in extreme and normal rainfall events.

799 The indirect effect is positive even for normal rainfall events because although average water  
800 vapor concentration in normal rainfall events is lower in comparison to the extreme rainfall  
801 events, the water vapor concentration is still high enough for droplets to grow from the moisture  
802 supplied by the sea breezes on a diurnal basis. So given the abundant moisture supply, there is

803 relatively minimal competition of raindrops, rendering the indirect effect to be positive even  
804 during the normal rainfall events.

805 The relative sign and magnitude of the observed effects are meaningful. The indirect effects are  
806 similar in both extreme and normal rainfall events (4.54% vs. 4.76%), which is reasonable  
807 because the indirect effect does not depend upon the breeze system. The direct effect is  
808 considerably stronger for normal rainfall events (-5.78%) than that for extreme rainfall events  
809 (1.51%), which is also reasonable because the rainfall in normal rainfall is governed by breeze  
810 circulation whereas for extreme rainfall events it is not. Physically, the direct effect in the  
811 extreme rainfall events is governed by diverse synoptic processes and breezes do not play a  
812 significant role in the effect.

813 Dust can direct and indirect effects both contribute in modifying the cloud properties through  
814 both direct and indirect effects. The indirect effects are positive because the dust directly  
815 contributes to the formation of CCN. Figure This is evident in Fig. S2b presents the total,  
816 indirect, and direct effect of dust on cloud water mixing ratio at a cloud-level height (4.6 km).  
817 Statistically, which shows a statistically significant increase in cloud water mixing ratios is  
818 observed over the lands due to the indirect effects (Fig. S2b). As expected, the changes in clouds  
819 caused by the dust direct effects are not statistically significant in most areas (Fig. S2c). Dust  
820 indirect effects are more complex but aerosols are known to suppress rainfall at the initial stage  
821 of convection and enhances rainfall during the mature stage through aerosol invigoration  
822 (Andreae et al., 2004; Koren et al., 2005; Koren et al., 2008; Chakraborty et al., 2018; Fan et al.,  
823 2018). Increased aerosol concentration can also increase cloud-top evaporation, thus reducing the  
824 cloud coverage (Choobari, 2018). Similar to dust direct effects,

825 Dust indirect effect also evidently induces significant surface cooling and warming through  
826 clouds through indirect effects as well (Fig. 13b), as clouds also scatter and absorb shortwave  
827 radiation similar to dust.

828 Therefore, we concluded that the rain suppression (enhancement) over the study region is  
829 governed primarily by dust induced land surface cooling (warming) either directly or through  
830 clouds, which ultimately decreases (increases) landward moisture transport by weakening  
831 (strengthening) sea breeze circulation. It is also worth noting that the net effect of dust on surface  
832 temperature through clouds depends on the cloud heights and other cloud properties.

833 In this study, we evaluated the relative contribution of direct and indirect effects of dust on  
834 rainfall and explored associated physical mechanisms using well-developed microphysical and  
835 aerosol schemes in WRF-Chem. Modeling rainfall processes entails some uncertainty, which is  
836 mainly related to the effect of aerosols on clouds. We indeed observed a large order of difference  
837 in simulated microphysical parameters (CCN # concentrations and aerosol size distributions)  
838 compared to observations, although they did not have much impact on the rainfall in the study  
839 region. There are several microphysical processes governing dust-cloud-rainfall interactions that  
840 are not fully understood or implemented yet in WRF-Chem (e.g., the prognostic treatment of ice  
841 nucleation by dust) (Chapman et al., 2009). Therefore, our model simulations may have not

Formatted: Font color: Red

842 captured some dust-cloud-rainfall interactions occurring in reality, particularly those related to  
843 cold-cloud processes.

844 ~~This order of difference, although large, is reasonable for microphysical parameters given the~~  
845 ~~high uncertainty in their parameterization.~~

#### 846 *Broader implications*

847 Through high-resolution model simulations, complemented with multiple observational data, we  
848 investigated how dust affects rainfall over the Red Sea coastal region through direct and indirect  
849 effects. Our study has broader social and environmental implications. While dust and dust storms  
850 are generally considered detrimental from an air quality perspective, our study highlights their  
851 contribution in modulating rain, an essential element of plant and animal life. A Better  
852 understanding of regional rainfall process can be helpful for planning and managing regional  
853 water resources as the replenishment of surface and ground water largely depends on  
854 precipitation (Mostamandi et al., 2020). A better understanding of the dynamics of extreme  
855 rainfall events could also aid in the development of strategies to minimize their catastrophic  
856 outcomes such as heavy flooding and loss of public property (e.g., de Vries et al., 2013). Recent  
857 studies suggest that there is an increase in the dust/aerosol activity in the region (e.g.,  
858 Klingmüller et al., 2016). In this context, our model experiments (no\_dust and all\_aer) can also  
859 provide insights into how increased dust activity affects regional rainfall patterns.

860 Our study also has implications from a cloud-seeding perspective, which is relevant in the  
861 context of recent rainfall enhancement efforts over the region (e.g., Yanlong et al., 2017;  
862 [Mazroui and Farrah, 2017](#)). Cloud seeding experiments were conducted in the southwest of  
863 Saudi Arabia in the Asir mountainous region in 2006–2008 using AgI, which receives a  
864 relatively high amount of precipitation (Sinkevich and Krauss, 2010). Those results  
865 demonstrated the feasibility of cloud seeding over the region by showing that the reflectivity of  
866 seeded clouds was significantly different compared to that of natural clouds (Sinkevich and  
867 Krauss, 2010; Krauss et al., 2011). However, our results suggest that cloud seeding efficiency  
868 may be affected by the presence of background dust aerosols, and that ~~it may not be cloud~~  
869 ~~seeding using commonly used materials such as AgI may not be~~ as effective in dusty regions as  
870 in clean environments. It should also be noted that the effectiveness of cloud seeding depends  
871 upon the height of application. Therefore, before investing on expensive field experiments on  
872 cloud seeding, it would be beneficial to evaluate the effectiveness of cloud seeding through  
873 regional modeling in the areas of interest as done in this study.

#### 874 **5. Conclusion**

875 Our study evaluated the effect of dust on rainfall over the Red Sea coastal plains using a double-  
876 moment microphysics scheme (Morrison) combined with an advanced aerosol scheme  
877 (MOSAIC) in WRF-Chem. The model captured the magnitude of AOD and aerosol vertical  
878 profiles, the vertical profile of air temperature, the diurnal cycle of winds, spatio-temporal  
879 variation of accumulated rainfall, and the CCN number concentrations over the study domain  
880 reasonably well.

881 The rainfall over the Red Sea coast is mainly governed by warm cloud processes, which mainly  
882 occur within a ~5 km height. Rainfall has a strong diurnal cycle, which peaks in the evening at  
883 approximately 15:00 UTC (6 pm local time) under the influence of sea breezes.

884 We calculated the total, direct, and indirect effects of dust on rainfall for extreme and normal  
885 rainfall events in terms of the 10-year (2006–2015) August average daily-accumulated rainfall  
886 over the study domain (d03). For extreme rainfall events (average daily-accumulated rainfall  $\geq$   
887 1.33 mm), dust causes a net enhancement on rainfall of 0.140 mm (6.05%), whereas the indirect  
888 and the direct effects accounted for 0.105 mm (4.54 %) and 0.035 mm (1.51 %), respectively.  
889 Although the positive direct effect is statistically insignificant at the assumed 5% significance  
890 level, it adds up with the positive indirect effect, making the total effect significant. For the  
891 normal rainfall events (average daily-accumulated rainfall  $<$  1.33 mm), dust causes a net  
892 suppression of rainfall of -0.003 mm (-1.02 %), with the indirect and direct effects accounting for  
893 0.014 (4.76 %), and -0.017 mm (-5.78 %), respectively, all of which were statistically significant.  
894 The indirect and direct effects, which are opposite in sign and nearly equal in magnitude, cancel  
895 each other out, making the total effect small but statistically significant.

896 Dust affects rainfall over the Red Sea coastal region through both direct and indirect effects. For  
897 normal rainfall events, dust suppresses rainfall by direct effects through the weakening of sea  
898 breeze circulation, caused by dust- by influencing the sea-breeze circulation induced. -Dust  
899 induces land surface cooling. Such weakening of sea breezes reduces the landward moisture  
900 transport, which ultimately caused by shortwave scattering and warming caused mainly by  
901 shortwave absorption, which are further modulated by its effect on clouds. Such land cooling  
902 (warming) ultimately weakens (strengthens) the sea breeze circulation, thus reducing  
903 (increasing) the landward moisture transport and suppresses the ssing (enhancing) coastal  
904 rainfall. For extreme rainfall events, the dust effect on breezes become smaller and dust causes  
905 net rainfall enhancement through the indirect effects given the abundance of water vapor and  
906 dust concentrations over the study site, which facilitates raindrops to grow larger.

907 Given that the study area exhibit stable breeze circulation, our results could be extended to other  
908 coastal areas with a topography that have similar breeze system. Importantly, our results have  
909 broader scientific and environmental implications. Although dust is considered a nuisance from  
910 an air quality perspective, our results highlight the more positive fundamental role of dust  
911 particles in modulating rainfall formation and distribution. In the context of regional rain  
912 enhancement efforts, our results also have implications for cloud seeding and regional water  
913 resource management.

914  
915 *Codes and data availability.* MODIS AOD data were downloaded from  
916 <http://ladsweb.nascom.nasa.gov/data/>. MERRA-2 and IMERG data were obtained from the  
917 NASA Goddard Earth Sciences Data and Information Services Center (GES DISC) available at  
918 <https://disc.gsfc.nasa.gov/>. ECMWF Operational Analysis data are restricted data, which were  
919 retrieved from [http://apps.ecmwf.int/archive-](http://apps.ecmwf.int/archive-catalogue/?type=4v&class=od&stream=oper&expver=1)  
920 [catalogue/?type=4v&class=od&stream=oper&expver=1](http://apps.ecmwf.int/archive-catalogue/?type=4v&class=od&stream=oper&expver=1) with a membership. EDGAR-4.2 is

921 available at <http://edgar.jrc.ec.europa.eu/overview.php?v=42>. Field observation data and VIIRS  
922 satellite data may be obtained by request to the first author at [psagar@utexas.edu](mailto:psagar@utexas.edu). A copy of the  
923 namelist.input file with details of the WRF-Chem model configuration can be downloaded from  
924 the KAUST repository at <http://hdl.handle.net/10754/675620>.

925 *Acknowledgements.* Our study was supported by funding from King Abdullah University of  
926 Science and Technology (KAUST). We also thank Dr. Daniel Rosenfeld for his assistance in the  
927 acquisition of VIIRS data. Battelle Memorial Institute operates PNNL under contract DEAC05-  
928 76RL01830.

929 *Author contributions.* SPP and GLS developed the central scientific concept of the paper. SPP  
930 analyzed the data and wrote the paper with inputs from GLS. SPP conducted the WRF-Chem  
931 simulations, and AU contributed with code modifications. PK and DA processed and provided  
932 data from the August 2009 field campaign in Saudi Arabia. YZ processed and provided the  
933 VIIRS data. All authors discussed the results and contributed to the final manuscript.

934 *Competing interests.* The authors declare that they have no conflict of interest.

935



936 **References**

- 937 Abdul-Razzak, H., and Ghan, S. J., A parameterization of aerosol activation, 3, Sectional representation,  
938 J. Geophys. Res., 107(D3), doi:10.1029/2001JD000483, 2002.
- 939 Andreae, M.O., Rosenfeld, D., Artaxo, P., Costa, A.A., Frank, G.P., Longo, K.M. and Silva-Dias, M.D.:  
940 Smoking rain clouds over the Amazon, Science, 303(5662), 1337-1342,  
941 <https://doi.org/10.1126/science.1092779>, 2004.
- 942 Abbott, T. H. and Cronin, T. W.: Aerosol invigoration of atmospheric convection through increases in  
943 humidity, Science, 371 (6524), 83-85, <https://doi.org/10.1126/science.abc5181>, 2021.
- 944 Aina, Y.A., Van der Merwe, J. H. and Alshuwaikhat, H.M.: Spatial and Temporal Variations of Satellite-  
945 Derived Multi-Year Particulate Data of Saudi Arabia: An Exploratory Analysis. International  
946 Journal of Environmental Research and Public Health, 11, 11,152-11,166.  
947 <https://doi.org/10.3390/ijerph11111152>, 2014.
- 948 Alam, M.M.: Impact of cloud microphysics and cumulus parameterization on simulation of heavy rainfall  
949 event during 7–9 October 2007 over Bangladesh, Journal of earth system science, 123(2), 259-  
950 279, <https://doi.org/10.1007/s12040-013-0401-0>, 2014.
- 951 Albrecht, B.A.: Aerosols, cloud microphysics, and fractional cloudiness, Science, 245(4923), 1227-1230,  
952 <https://doi.org/10.1126/science.245.4923.1227>, 1989.
- 953 [Almazroui, M. and Saeed, S.: Contribution of extreme daily precipitation to total rainfall over the Arabian  
954 Peninsula, Atmospheric Research, 231, 104672, https://doi.org/10.1016/j.atmosres.2019.104672,  
955 2020.](https://doi.org/10.1016/j.atmosres.2019.104672)
- 956 Ansmann, A., Mattis, I., Müller, D., Wandinger, U., Radlach, M., Althausen, D., et al.: Ice formation in  
957 Saharan dust over central Europe observed with temperature/humidity/aerosol Raman lidar,  
958 Journal of Geophysical Research, 110, D18S12, <https://doi.org/10.1029/2004jd005000>, 2005.
- 959 Anisimov, A., Tao, W., Stenchikov, G., Kalenderski, S., Prakash, P. J., Yang, Z.-L., and Shi, M.:  
960 Quantifying local-scale dust emission from the Arabian Red Sea coastal plain, Atmospheric  
961 Chemistry and Physics, 17, 993–1015, <https://doi.org/10.5194/acp-17-993-2017>, 2017.
- 962 Bangalath, H. K., and Stenchikov, G. (2015), Role of dust direct radiative effect on the tropical rain belt  
963 over Middle East and North Africa: A high-resolution AGCM study, J. Geophys. Res. Atmos.,  
964 120, 4564– 4584. doi:10.1002/2015JD023122.
- 965 Bond, T. C., et al.: Bounding the role of black carbon in the climate system: A scientific assessment,  
966 Journal of Geophysical Research, 118(11), 5380–5552, <https://doi.org/10.1002/jgrd.50171>, 2013.
- 967 Chakraborty, S., Fu, R., Rosenfeld, D., & Massie, S. T.: The influence of aerosols and meteorological  
968 conditions on the total rain volume of the mesoscale convective systems over tropical continents,  
969 Geophysical Research Letters, 45, 13,099– 13,106. <https://doi.org/10.1029/2018GL080371>, 2018.
- 970 Chapman, E. G., Gustafson Jr, W. I., Easter, R. C., Barnard, J. C., Ghan, S. J., Pekour, M. S., et al.:  
971 Coupling aerosol-cloud-radiative processes in the WRF-Chem model: Investigating the radiative  
972 impact of elevated point sources, Atmospheric Chemistry and Physics, 9(3), 945-964,  
973 <https://doi.org/10.5194/acp-9-945-2009>, 2009.
- 974 Choobari, O.A., Zawar-Reza, P. and Sturman, A.: The global distribution of mineral dust and its impacts  
975 on the climate system: A review, Atmospheric Research, 138, 152-165,  
976 <https://doi.org/10.1016/j.atmosres.2013.11.007>, 2014.
- 977 Choobari, O., A.: Impact of aerosol number concentration on precipitation under different precipitation  
978 rates. Meteorological Applications, 25, 596– 605, <https://doi.org/10.1002/met.1724>, 2018.
- 979 Choudhury, G., Tyagi, B., Vissa, N. K., Singh, J., Sarangi, C., Tripathi, S. N., and Tesche, M.: Aerosol-  
980 enhanced high precipitation events near the Himalayan foothills, Atmospheric Chemistry and  
981 Physics, 20, 15389–15399, <https://doi.org/10.5194/acp-20-15389-2020>, 2020.
- 982 Creamean, J. M., Suski, K. J., Rosenfeld, D., Cazorla, A., DeMott, P. J., Sullivan, R. C., et al.: Dust and  
983 biological aerosols from the Sahara and Asia influence precipitation in the Western U.S, Science,  
984 339(6127), 1572–1578, <https://doi.org/10.1126/science.1227279>, 2013.

985 Dagan, G., Koren, I., and Altaratz, O.: Competition between core and periphery-based processes in warm  
986 convective clouds – from invigoration to suppression, *Atmospheric Chemistry and Physics*, 15,  
987 2749–2760, <https://doi.org/10.5194/acp-15-2749-2015>, 2015.

988 Deng, L., McCabe, M. F., Stenchikov, G., Evans, J. P., and P. A. Kucera, P. A.: Simulation of Flash-  
989 Flood-Producing Storm Events in Saudi Arabia Using the Weather Research and Forecasting  
990 Model, *Journal of Hydrometeorology*, 16, 615–630, <https://doi.org/10.1175/JHM-D-14-0126.1>,  
991 2015.

992 Dennis, A.S.: Weather modification by cloud seeding, *International geophysics series*, 24, 670,  
993 [https://digitalcommons.usu.edu/water\\_rep/670](https://digitalcommons.usu.edu/water_rep/670), 1980.

994 Deshler, T., Reynolds, D. W. and Huggins, A. W.: Physical Response of Winter Orographic Clouds over  
995 the Sierra Nevada to Airborne Seeding Using Dry Ice or Silver Iodide, *Journal of Applied  
996 Meteorology*, 29, 288–330, [https://doi.org/10.1175/1520-  
997 0450\(1990\)029<0288:PROWOC>2.0.CO;2](https://doi.org/10.1175/1520-0450(1990)029<0288:PROWOC>2.0.CO;2), 1990.

998 de Vries, A. J., Tyrlis, E., Edry, D., Krichak, S. O., Steil, B., and Lelieveld, J.: Extreme precipitation  
999 events in the Middle East: Dynamics of the Active Red Sea Trough, *Journal of Geophysical  
1000 Research*, 118, 7087–7108, <https://doi.org/10.1002/jgrd.50569>, 2013.

1001 Dubovik, O., Herman, M., Holdak, A., Lapyonok, T., Tanré, D., Deuzé, J. L., Ducos, F., Sinyuk, A., and  
1002 985 Lopatin, A.: Statistically optimized inversion algorithm for enhanced retrieval of aerosol 986  
1003 properties from spectral multi-angle polarimetric satellite observations, *Atmos. Meas. Tech.*, 4,  
1004 987 975–1018, <https://doi.org/10.5194/amt-4-975-2011>, 2011.

1005 Dye, J. E., & Baumgardner, D. (1984). Evaluation of the Forward Scattering Spectrometer Probe. Part I:  
1006 Electronic and Optical Studies, *Journal of Atmospheric and Oceanic Technology*, 1(4), 329-344.  
1007 Retrieved Sep 14, 2021, from [https://journals.ametsoc.org/view/journals/atot/1/4/1520-  
1008 0426\\_1984\\_001\\_0329\\_eotfss\\_2\\_0\\_co\\_2.xml](https://journals.ametsoc.org/view/journals/atot/1/4/1520-0426_1984_001_0329_eotfss_2_0_co_2.xml).

1009 Eck, T. F., et al.: Spatial and temporal variability of column-integrated aerosol optical properties in the  
1010 southern Arabian Gulf and United Arab Emirates in summer, *Journal of Geophysical Research*,  
1011 113, D01204, <https://doi.org/10.1029/2007JD008944>, 2008.

1012 Fan, J., Rosenfeld, D., Zhang, Y., Giangrande, S.E., Li, Z., Machado, L.A., Martin, S.T., Yang, Y., Wang,  
1013 J., Artaxo, P. and Barbosa, H.M.: Substantial convection and precipitation enhancements by  
1014 ultrafine aerosol particles, *Science*, 359 (6374), 411-418,  
1015 <https://doi.org/10.1126/science.aan8461>, 2018.

1016 Farrar, J., Lentz, S., Churchill, J., Bouchard, P., Smith, J., Kemp, J., Lord, J., Allsup, G., and Hosom, D.:  
1017 King Abdullah University of Science and Technology (KAUST) mooring deployment cruise and  
1018 fieldwork report, Technical report, Woods Hole Oceanographic Institution, WHOI-KAUST-  
1019 CTR-2009, 2, 2009.

1020 Fast, J. D., Gustafson, W. I., Easter, R. C., Zaveri, R. A., Barnard, J. C., Chapman, E. G., Grell, G. A.,  
1021 and Peckham, S. E.: Evolution of ozone, particulates, and aerosol direct radiative forcing in the  
1022 vicinity of Houston using a fully coupled meteorology-chemistry-aerosol model, *Journal of  
1023 Geophysical Research*, 111, D21305, <https://doi.org/10.1029/2005JD006721>, 2006.

1024 Forkel, R., Werhahn, J., Hansen, A. B., McKeen, S., Peckham, S., Grell, G., et al.: Effect of aerosol-  
1025 radiation feedback on regional air quality – A case study with WRF/Chem, *Atmospheric  
1026 Environment*, 53, 202-211, <https://doi.org/10.1016/j.atmosenv.2011.10.009>, 2012.

1027 Gao, W., Fan, J., Easter, R. C., Yang, Q., Zhao, C., and Ghan, S. J.: Coupling spectral-bin cloud  
1028 microphysics with the MOSAIC aerosol model in WRF-Chem: Methodology and results for  
1029 marine stratocumulus clouds, *Journal of Advances in Modeling Earth Systems*, 8, 1289–1309,  
1030 <https://doi.org/10.1002/2016MS000676>, 2016.

1031 Georgoulias, A.K., Marinou, E., Tsekeri, A., Proestakis, E., Akritidis, D., Alexandri, G., et al.: A First  
1032 Case Study of CCN Concentrations from Spaceborne Lidar Observations, *Remote  
1033 Sensing*, 12(10), 1557, <https://doi.org/10.3390/rs12101557>, 2020.

1034 Gibbons, J. D. and Chakraborti, S.: *Nonparametric Statistical Inference*, 5th Ed., Boca Raton, FL:  
1035 Chapman & Hall/CRC Press, Taylor & Francis Group, 2011.

1036 Grabowski, W. W., and Morrison, H.: Do Ultrafine Cloud Condensation Nuclei Invigorate Deep  
1037 Convection? *Journal of the Atmospheric Sciences*, 77(7), 2567-2583,  
1038 <https://doi.org/10.1175/JAS-D-20-0012.1>, 2020.

1039 Grell, G.A., Peckham, S.E., Schmitz, R., McKeen, S.A., Frost, G., Skamarock, W.C. and Eder, B.: Fully  
1040 coupled “online” chemistry within the WRF model. *Atmospheric Environment*, 39(37), pp.6957-  
1041 6975, <https://doi.org/10.1016/j.atmosenv.2005.04.027>, 2005.

1042 Gustafson, W. I., Chapman, E. G., Ghan, S. J., Easter, R. C., and Fast, J. D. (2007): Impact on modeled  
1043 cloud characteristics due to simplified treatment of uniform cloud condensation nuclei during  
1044 NEAQS 2004, *Geophysical Research Letters*, 34, L19809,  
1045 <https://doi.org/10.1029/2007GL030021>, 2007.

1046 Han, Y., Fang, X., Zhao, T., Bai, H., Kang, S., and Song, L.: Suppression of precipitation by dust  
1047 particles originated in the Tibetan Plateau, *Atmospheric Environment*, 43(3), 568-574,  
1048 <https://doi.org/10.1016/j.atmosenv.2008.10.018>, 2009.

1049 Hansen, J., Sato, M. and Ruedy, R.: Radiative forcing and climate response. *Journal of Geophysical*  
1050 *Research: Atmospheres*, 102(D6), 6831-6864, <https://doi.org/10.1029/96JD03436>, 1997.

1051 Held, I. M., and Soden, B. J.: Robust Responses of the Hydrological Cycle to Global Warming, *Journal of*  
1052 *Climate*, 19(21), 5686-5699,  
1053 <https://journals.ametsoc.org/view/journals/clim/19/21/jcli3990.1.xml>, 2006.

1054 Herich, H.; Tritscher, T.; Wiacek, A.; Gysel, M.; Weingartner, E.; Lohmann, U.; Baltensperger, U.;  
1055 Cziczo, D. J.: Water Uptake of Clay and Desert Dust Aerosol Particles at Sub- and Supersaturated  
1056 Water Vapor Conditions, *Physical Chemistry Chemical Physics*, 11, 7804– 7809,  
1057 <https://doi.org/10.1039/B901585J>, 2009.

1058 Hollander, M. and Wolfe, D. A.: *Nonparametric Statistical Methods*, Hoboken, NJ: John Wiley & Sons,  
1059 Inc., 1999.

1060 Hong, S.-Y., Yign N., and Dudhia, J.: A new vertical diffusion package with an explicit treatment of  
1061 entrainment processes, *Monthly Weather Review*, 134, 2318–2341,  
1062 <https://doi.org/10.1175/MWR3199.1>, 2006.

1063 Huffman, G.J., E.F. Stocker, D.T. Bolvin, E.J. Nelkin, Jackson Tan (2019), GPM IMERG Late  
1064 Precipitation L3 1 day 0.1 degree x 0.1 degree V06, Edited by Andrey Savtchenko, Greenbelt,  
1065 MD, Goddard Earth Sciences Data and Information Services Center (GES DISC), Accessed: [Sep  
1066 12, 2021], 10.5067/GPM/IMERGDL/DAY/06.

1067 Iacono, M. J., Delamere, J. S., Mlawer, E. J., Shephard, M. W., Clough, S. A. and Collins, W. D.:  
1068 Radiative forcing by long-lived greenhouse gases: Calculations with the AER radiative transfer  
1069 models, *Journal of Geophysical Research*, 113, D13103, <https://doi.org/10.1029/2008JD009944>,  
1070 2008.

1071 IPCC Climate Change 2013: The Physical Science Basis. Contribution of Working Group I to the Fifth  
1072 Assessment Report of the Intergovernmental Panel on Climate Change [Stocker, T.F., D. Qin, G.-  
1073 K. Plattner, M. Tignor, S.K. Allen, J. Boschung, A. Nauels, Y. Xia, V. Bex and P.M. Midgley  
1074 (eds.)], Cambridge University Press, Cambridge, United Kingdom and New York, NY, USA,  
1075 1535, <https://www.ipcc.ch/report/ar5/wg1/>, 2013.

1076 Jacobson, M. Z. and Kaufman, Y. J.: Wind reduction by aerosol particles, *Geophysical Research*  
1077 *Letters*, 33, L24814, <https://doi.org/10.1029/2006GL027838>, 2006.

1078 [Janssens-Maenhout, G., Crippa, M., Guizzardi, D., Dentener, F., Muntean, M., Pouliot, G., Keating, T.,  
1079 Zhang, Q., Kurokawa, J., Wankmüller, R., Denier van der Gon, H., Kuenen, J. J. P., Klimont, Z.,  
1080 Frost, G., Darras, S., Koffi, B., and Li, M.: HTAP v2.2: a mosaic of regional and global emission  
1081 grid maps for 2008 and 2010 to study hemispheric transport of air pollution, \*Atmos. Chem. Phys.\*,  
1082 15, 11411–11432, <https://doi.org/10.5194/acp-15-11411-2015>, 2015.](https://doi.org/10.5194/acp-15-11411-2015)

1083 [Jha, V., Cotton, W., R., Carrió, G. G., and Walko, R.: Sensitivity Studies on the Impact of Dust and  
1084 Aerosol Pollution Acting as Cloud Nucleating Aerosol on Orographic Precipitation in the  
1085 Colorado River Basin, \*Advances in Meteorology\*, 3041893,  
1086 <https://doi.org/10.1155/2018/3041893>, 2018.](https://doi.org/10.1155/2018/3041893)

1087 Jha, V., Cotton, W. R., Carrió, G. G., Robert Walko, R. (2021) Seasonal estimates of the impacts of  
1088 aerosol and dust pollution on orographic precipitation in the Colorado River Basin, *Physical*  
1089 *Geography*, 42(1), 73-97, <https://doi.org/10.1080/02723646.2020.1792602>, 2021.

1090 Jin, Q., Wei, J., Yang, Z.-L., Pu, B., and Huang, J.: Consistent response of Indian summer monsoon to  
1091 Middle East dust in observations and simulations, *Atmos. Chem. Phys.*, 15, 9897–9915,  
1092 <https://doi.org/10.5194/acp-15-9897-2015>, 2015.

1093 Jones, C., Mahowald, N. and Luo, C.: Observational evidence of African desert dust intensification of  
1094 easterly waves, *Geophysical Research Letters*, 31, L17208, <https://doi.org/10.1029/2004GL020107>,  
1095 [2004](https://doi.org/10.1029/2004GL020107).

1096 Joodaki, G., Wahr, J., and Swenson, S.: Estimating the human contribution to groundwater depletion in  
1097 the Middle East, from GRACE data, land surface models, and well observations, *Water*  
1098 *Resources Research*, 50, 2679–2692, <https://doi.org/10.1002/2013WR014633>, 2014.

1099 Jordan, A. K., Zaitchik, B. F., Gnanadesikan, A., Kim, D., and Badr, H. S.: Strength of Linkages Between  
1100 Dust and Circulation Over North Africa: results from a coupled modeling system with active  
1101 dust, *Journal of Geophysical Research: Atmospheres*, 125, e2019JD030961,  
1102 <https://doi.org/10.1029/2019JD030961>, 2020.

1103 [Kalenderski, S., and Stenchikov, G. \(2016\). High-resolution regional modeling of summertime transport](https://doi.org/10.1002/2015JD024480)  
1104 [and impact of African dust over the Red Sea and Arabian Peninsula, \*J. Geophys. Res. Atmos.\*,](https://doi.org/10.1002/2015JD024480)  
1105 [121, 6435–6458, doi:10.1002/2015JD024480.](https://doi.org/10.1002/2015JD024480)

1106 [Kawecki, S., & Steiner, A. L. \(2018\). The influence of aerosol hygroscopicity on precipitation intensity](https://doi.org/10.1002/2017JD026535)  
1107 [during a mesoscale convective event. \*Journal of Geophysical Research: Atmospheres\*, 123, 424–](https://doi.org/10.1002/2017JD026535)  
1108 [442. <https://doi.org/10.1002/2017JD026535>](https://doi.org/10.1002/2017JD026535)

1109 [Karydis, V. A., Kumar, P., Barahona, D., Sokolik, I. N., and Nenes, A. \(2011\). On the effect of dust](https://doi.org/10.1029/2011JD016283)  
1110 [particles on global cloud condensation nuclei and cloud droplet number, \*J. Geophys. Res.\*, 116,](https://doi.org/10.1029/2011JD016283)  
1111 [D23204, doi:10.1029/2011JD016283.](https://doi.org/10.1029/2011JD016283)

1112 [Keith, D. W., Weisenstein, D. K., Dykema, J. A. & Keutsch, F. N. Stratospheric solar geoengineering](https://doi.org/10.1073/pnas.1615572113)  
1113 [without ozone loss. \*Proc. Natl Acad. Sci.\* 113, 14910–14914 \(2016\),](https://doi.org/10.1073/pnas.1615572113)  
1114 [https://doi.org/10.1073/pnas.1615572113.](https://doi.org/10.1073/pnas.1615572113)

1115 Khan, B., Stenchikov, G., Weinzierl, B., Kalenderski, S., and Osipov, S.: Dust plume formation in the  
1116 free troposphere and aerosol size distribution during the Saharan Mineral Dust Experiment in  
1117 North Africa, *Tellus B: Chemical and Physical Meteorology*, 67(1),  
1118 <https://doi.org/10.3402/tellusb.v67.27170>, 2015.

1119 Konare, A., Zakey, A. S., Solmon, F., Giorgi, F., Rauscher, S., Ibrah, S., et al.: A regional climate  
1120 modeling study of the effect of desert dust on the West African monsoon, *Journal of Geophysical*  
1121 *Research*, 113, D12206, <https://doi.org/10.1029/2007JD009322>, 2008.

1122 Koehler, K. A., Kreidenweis, S. M., DeMott, P. J., Petters, M. D., Prenni, A. J., and Carrico, C. M.:  
1123 Hygroscopicity and cloud droplet activation of mineral dust aerosol, *Geophysical Research*  
1124 *Letters*, 36, L08805, <https://doi.org/10.1029/2009GL037348>, 2009.

1125 Klingmüller, K., Karydis, V. A., Bacer, S., Stenchikov, G. L., and Lelieveld, J.: Weaker cooling by  
1126 aerosols due to dust–pollution interactions, *Atmospheric Chemistry and Physics*, 20, 15285–  
1127 15295, <https://doi.org/10.5194/acp-20-15285-2020>, 2020.

1128 Klingmüller, K., Lelieveld, J., Karydis, V. A., and Stenchikov, G. L.: Direct radiative effect of dust–  
1129 pollution interactions, *Atmos. Chem. Phys.*, 19, 7397–7408, [https://doi.org/10.5194/acp-19-7397-](https://doi.org/10.5194/acp-19-7397-2019)  
1130 [2019](https://doi.org/10.5194/acp-19-7397-2019), 2019.

1131 Klingmüller, K., Pozzer, A., Metzger, S., Stenchikov, G. L., and Lelieveld, J.: Aerosol optical depth trend  
1132 over the Middle East, *Atmospheric Chemistry and Physics*, 16, 5063–5073,  
1133 <https://doi.org/10.5194/acp-16-5063-2016>, 2016.

1134 Kondapalli, N. K. and Suzuki, K.: Assessment of seasonal cloud properties in the United Arab Emirates  
1135 and adjoining regions from geostationary satellite data, *Remote Sensing of Environment*, 228, 90–  
1136 104, <https://doi.org/10.1016/j.rse.2019.04.024>, 2019.

1137 Koren, I., Kaufman, Y. J., Rosenfeld, D., Remer, L. A., and Rudich, Y.: Aerosol invigoration and  
1138 restructuring of Atlantic convective clouds, *Geophysical Research Letters*, 32, L14828,  
1139 <https://doi.org/10.1029/2005GL023187>, 2005.

1140 Koren, I., Martins, J.V., Remer, L.A. and Afargan, H.: Smoke invigoration versus inhibition of clouds  
1141 over the Amazon, *Science*, 321(5891), 946-949, <https://doi.org/10.1126/science.1159185>, 2008.

1142 Koren, I., Dagan, G. and Altaratz, O.: From aerosol-limited to invigoration of warm convective clouds,  
1143 *Science*, 344(6188), 1143-1146, <https://doi.org/10.1126/science.1252595>, 2014.

1144 Krauss, T.W., Sinkevich, A.A. and Ghulam, A.S.: Effects of feeder cloud merging on storm development  
1145 in Saudi Arabia, *Journal of King Abdulaziz University: Metrology, Environment and Arid Land*  
1146 *Agricultural Sciences*, 142(592), 1-33, <https://doi.org/10.4197/Met.22-2.2>, 2011.

1147 Kucera, P., Axisa, D., Burger, R.P., Collins, D.R., Li, R., Chapman, M., et al.: Features of the Weather  
1148 Modification Assessment Project in Southwest Region of Saudi Arabia, *The Journal of Weather*  
1149 *Modification*, 42(1), 78-103, 2010.

1150 Lau, W. K. M., Kim, M.-K., Kim, K.-M. and Lee, W.-S.: Enhanced surface warming and accelerated  
1151 snow melt in the Himalayas and Tibetan Plateau induced by absorbing aerosols, *Environmental*  
1152 *Research Letters*, 5, 025204, <https://doi.org/10.1088/1748-9326/5/2/025204>, 2010.

1153 Lee, S.S.: Effect of Aerosol on Circulations and Precipitation in Deep Convective Clouds, *Journal of*  
1154 *Atmospheric Science*, 69, 1957–1974, <https://doi.org/10.1175/JAS-D-11-0111.1>, 2012, 2012.

1155 Li, R., Min, Q. and Harrison, L. C.: A Case Study: The Indirect Aerosol Effects of Mineral Dust on Warm  
1156 Clouds, *Journal of Atmospheric Science*, 67, 805–816, <https://doi.org/10.1175/2009JAS3235.1>,  
1157 2010.

1158 Li, Z., Niu, F., Fan, J., Liu, Y., Rosenfeld, D. and Ding, Y.: Long-term impacts of aerosols on the vertical  
1159 development of clouds and precipitation, *Nature Geoscience*, 4(12), 888-894,  
1160 <https://doi.org/10.1038/ngeo1313>, 2011.

1161 Lim, K. S., and Hong, S.: Development of an Effective Double-Moment Cloud Microphysics Scheme  
1162 with Prognostic Cloud Condensation Nuclei (CCN) for Weather and Climate Models, *Monthly*  
1163 *Weather Review*, 138, 1587-1612, <https://doi.org/10.1175/2009MWR2968.1>, 2010.

1164 Liu, Z., Ostrenga, D., Teng, W. and Kempler, S.: Tropical Rainfall Measuring Mission (IMERG)  
1165 Precipitation Data and Services for Research and Applications, *Bulletin of American*  
1166 *Meteorological Society*, 93, 1317–1325, <https://doi.org/10.1175/BAMS-D-11-00152.1>, 2012.

1167 Lohmann, U. and Feichter, J.: Can the direct and semi-direct aerosol effect compete with the indirect  
1168 effect on a global scale?, *Geophysical Research Letters*, 28(1), 159-161,  
1169 <https://doi.org/10.1029/2000GL012051>, 2001.

1170 [Lopatin, A., Dubovik, O., Fuertes, D., Stenchikov, G., Lapyonok, T., Veselovskii, I., Wienhold, F. G.,  
1171 Shevchenko, I., Hu, Q., and Parajuli, S.: Synergy processing of diverse ground-based remote  
1172 sensing and in situ data using GRASP algorithm: applications to radiometer, lidar and radiosonde  
1173 observations, \*Atmos. Meas. Tech. Discuss.\* \[preprint\], <https://doi.org/10.5194/amt-2020-422>, in  
1174 review, 2020.](https://doi.org/10.5194/amt-2020-422)

1175 [Mahmoud, M. T., Al-Zahrani, M. A. and Sharif, H. O.: Assessment of global precipitation measurement  
1176 satellite products over Saudi Arabia, \*Journal of Hydrology\*, 559, 1-12,  
1177 <https://doi.org/10.1016/j.jhydrol.2018.02.015>, 2018.](https://doi.org/10.1016/j.jhydrol.2018.02.015)

1178 Marengo, F., Ryder, C., Estellés, V., O'Sullivan, D., Brooke, J., Orgill, L., Lloyd, G., and Gallagher, M.:  
1179 Unexpected vertical structure of the Saharan Air Layer and giant dust particles during AER-D,  
1180 *Atmos. Chem. Phys.*, 18, 17655–17668, <https://doi.org/10.5194/acp-18-17655-2018>, 2018.

1181 [Mazroui, A.A. and Farrah, S.: The UAE seeks leading position in global rain enhancement research,  
1182 \*Journal of weather Modification\*, 49\(1\), 2017.](https://doi.org/10.1175/JWMODIF-D-16-0012.1)

1183 Michibata, T., and Takemura, T.: Evaluation of autoconversion schemes in a single model framework  
1184 with satellite observations, *Journal of Geophysical Research Atmospheres*, 120, 9570– 9590,  
1185 <https://doi.org/10.1002/2015JD023818>, 2015.

1186 Miller, S. T. K., Keim, B. D., Talbot, R. W., and Mao, H.: Sea breeze: Structure, forecasting, and impacts,  
1187 *Reviews of Geophysics*, 41, 1011, <https://doi.org/10.1029/2003RG000124>, 2003.

1188 Morrison, H., Thompson, G. and Tatarskii, V.: Impact of Cloud Microphysics on the Development of  
1189 Trailing Stratiform Precipitation in a Simulated Squall Line: Comparison of One- and Two-  
1190 Moment Schemes, *Monthly Weather Review*, 137, 991–  
1191 1007, <https://doi.org/10.1175/2008MWR2556.1>, 2009.

1192 Min, Q.-L., Li, R., Lin, B., Joseph, E., Wang, S. and Hu, Y. et al.: Evidence of mineral dust altering cloud  
1193 microphysics and precipitation, *Atmospheric Chemistry and Physics*, 9, 3223–3231,  
1194 <https://doi.org/10.5194/acp-9-3223-2009>, 2009.

1195 Mlawer, E. J., Taubman, S. J., Brown, P. D., Iacono, M. J., and Clough, S. A.: Radiative transfer for  
1196 inhomogeneous atmospheres: RRTM, a validated correlated-k model for the longwave, *Journal of*  
1197 *Geophysical Research*, 102( D14), 16663– 16682. <https://doi.org/10.1029/97JD00237>, 1997.

1198 Muhs, D. R.: The geologic records of dust in the Quaternary, *Aeolian Research*, 9, 3-48,  
1199 <https://doi.org/10.1016/j.aeolia.2012.08.001>, 2013.

1200 [Nazzari, Y., Barbulescu, A., Howari, F. et al.: New insights on sand dust storm from historical records, UAE, Arabian Journal of Geosciences, 12, 396, https://doi.org/10.1007/s12517-019-4555-1, 2019.](https://doi.org/10.1007/s12517-019-4555-1)

1201

1202

1203 Parajuli, S. P and Zender, C.: Connecting geomorphology to dust emission through high-resolution  
1204 mapping of global land cover and sediment supply, *Aeolian Research*, 27, 47-65,  
1205 doi:10.1016/j.aeolia.2017.06.002, 2017.

1206 Parajuli, S. P., Stenichikov, G. L., Ukhov, A., & Kim, H.: Dust emission modeling using a new high-  
1207 resolution dust source function in WRF-Chem with implications for air quality, *Journal of*  
1208 *Geophysical Research: Atmospheres*, 124, 10109–10133, <https://doi.org/10.1029/2019JD030248>,  
1209 2019.

1210 Parajuli, S. P., Stenichikov, G. L., Ukhov, A., Shevchenko, I., Dubovik, O., and Lopatin, A.: Aerosol  
1211 vertical distribution and interactions with land/sea breezes over the eastern coast of the Red Sea  
1212 from lidar data and high-resolution WRF-Chem simulations, *Atmos. Chem. Phys.*, 20, 16089–  
1213 16116, <https://doi.org/10.5194/acp-20-16089-2020>, 2020.

1214 Pu, B. and Ginoux, P.: Projection of American dustiness in the late 21st century due to climate change,  
1215 *Scientific Reports*, 7, 5553, <https://doi.org/10.1038/s41598-017-05431-9>, 2017,

1216 Rémy, S., Benedetti, A., Bozzo, A., Haiden, T., Jones, L., Razinger, M., et al.: Feedbacks of dust and  
1217 boundary layer meteorology during a dust storm in the eastern Mediterranean, *Atmospheric*  
1218 *Chemistry and Physics*, 15, 12909–12933, <https://doi.org/10.5194/acp-15-12909-2015>, 2015.

1219 [Rienecker, M. M., et al.: MERRA: NASA's modern-era retrospective analysis for research and applications, Journal of Climate, 24\(14\), 3624–3648, https://doi.org/10.1175/JCLI-D-11-00015.1, 2011.](https://doi.org/10.1175/JCLI-D-11-00015.1)

1220

1221

1222 [G. C. Roberts & A. Nenes \(2005\) A Continuous-Flow Streamwise Thermal-Gradient CCN Chamber for Atmospheric Measurements, Aerosol Science and Technology, 39:3, 206-221, DOI: 10.1080/027868290913988.](https://doi.org/10.1080/027868290913988)

1223

1224

1225 Robock, A., Bunzl, M., Kravitz, B. and Stenichikov, G.L.: A test for geoengineering?, *Science*, 327(5965),  
1226 530-531, <https://doi.org/10.1126/science.1186237>, 2010.

1227 Rosenfeld, D., Rudich, Y. Ronen Lahav, R.: Desert dust suppression precipitation: A possible  
1228 desertification feedback loop, *Proceedings of the National Academy of Sciences*, 98(11), 5975-  
1229 5980; <https://doi.org/10.1073/pnas.101122798>, 2001.

1230 Schulzweida, U., Kornbluh, L. and Quast, R.: CDO user's guide, *Climate data operators*, version 1(6),  
1231 2006.

1232 Shawon, A. S. M., Prabhakaran, P., Kinney, G., Shaw, R. A., and Cantrell, W.: Dependence of aerosol-  
1233 droplet partitioning on turbulence in a laboratory cloud, *Journal of Geophysical Research:*  
1234 *Atmospheres*, 126, e2020JD033799, <https://doi.org/10.1029/2020JD033799>, 2021.

1235 Sinkevich, A.A. and Krauss, T.W.: Cloud modification in Saudi Arabia: Statistical estimation of the  
1236 results, *Russian Meteorology and Hydrology*, 35, 378–385,  
1237 <https://doi.org/10.3103/S1068373910060038>, 2010.

1238 Simpson, J. E.: *Sea breeze and local winds*, Cambridge University Press, 1994.

1239 Solmon, F., Mallet, M., Elguindi, N., Giorgi, F., Zakey, A., and Konaré, A.: Dust aerosol impact on  
1240 regional precipitation over western Africa, mechanisms and sensitivity to absorption properties,  
1241 *Geophysical Research Letters*, 35, L24705, <https://doi.org/10.1029/2008GL035900>, 2008.

1242 Solomos, S., Kallos, G., Kushta, J., Astitha, M., Tremback, C., Nenes, A.: An integrated modeling study  
1243 on the effects of mineral dust and sea salt particles on clouds and precipitation, *Atmospheric*  
1244 *Chemistry and Physics*, 11, 873–892, <https://doi.org/10.5194/acp-11-873-2011>, 2011.

1245 Spurny, K. R.: Atmospheric Condensation Nuclei P. J. Coulier 1875 and J. Aitken 1880 (Historical  
1246 Review), *Aerosol Science and Technology*, 32:3, 243-248,  
1247 <https://doi.org/10.1080/027868200303777>, 2000.

1248 Stenchikov, G. L., Kirchner, I., Robock, A., Graf, H.-F., Antuña, J. C., Grainger, R. G., Lambert, A., and  
1249 Thomason, L.: Radiative forcing from the 1991 Mount Pinatubo volcanic eruption. *Journal of*  
1250 *Geophysical Research*, 103(D12), 13837– 13857. <https://doi.org/10.1029/98JD00693>, 1998.

1251 Stull, R. (2000). *Meteorology for scientists and engineers*. Brooks/Cole, 2000.

1252 Tang, M., Cziczo, D. J. and Grassian, V. H.: Interactions of Water with Mineral Dust Aerosol: Water  
1253 Adsorption, Hygroscopicity, Cloud Condensation, and Ice Nucleation, *Chemical Reviews*, 116  
1254 (7), 4205-4259, <https://doi.org/10.1021/acs.chemrev.5b00529>, 2016.

1255 Tewari, M., Chen, F., Wang, W., Dudhia, J., LeMone, M., Mitchell, K., Ek, M., Gayno, G., Wegiel, J.  
1256 and Cuenca, R. H.: Implementation and verification of the unified NOAH land surface model in  
1257 the WRF model, 20th conference on weather analysis and forecasting/16th conference on  
1258 numerical weather prediction, 11–15, 2004.

1259 Trinh, T.-A., Feeny, S. and Posso, A.: Rainfall shocks and child health: the role of parental mental health,  
1260 *Climate and Development*, <https://doi.org/10.1080/17565529.2020.1716672>, 2020.

1261 Tsvieli, Y. and Zangvil, A.: Synoptic climatological analysis of ‘wet’ and ‘dry’ Red Sea troughs over  
1262 Israel, *International Journal of Climatology*, 25(15), 1997–2015, <https://doi.org/10.1002/joc.123>,  
1263 2005.

1264 Tuccella, P., Curci, G., Grell, G. A., Visconti, G., Crumeyrolle, S., Schwarzenboeck, A., and Mensah, A.  
1265 A.: A new chemistry option in WRF-Chem v. 3.4 for the simulation of direct and indirect aerosol  
1266 effects using VBS: evaluation against IMPACT-EUCAARI data, *Geosci. Model Dev.*, 8, 2749–  
1267 2776, <https://doi.org/10.5194/gmd-8-2749-2015>, 2015.

1268 Twohy, C.H.: Measurements of Saharan Dust in Convective Clouds over the Tropical Eastern Atlantic  
1269 Ocean., *Journal of Atmospheric Science*, 72, 75–81, <https://doi.org/10.1175/JAS-D-14-0133.1>,  
1270 2015.

1271 Twomey, S. A.: Aerosols, clouds and radiation, *Atmospheric Environment, Part A*, 25, 2435-2442,  
1272 [https://doi.org/10.1016/0960-1686\(91\)90159-5](https://doi.org/10.1016/0960-1686(91)90159-5), 1991.

1273 Ukhov, A., Mostamandi, S., da Silva, A., Flemming, J., Alshehri, Y., Shevchenko, I., and Stenchikov, G.:  
1274 Assessment of natural and anthropogenic aerosol air pollution in the Middle East using MERRA-  
1275 2, CAMS data assimilation products, and high-resolution WRF-Chem model simulations,  
1276 *Atmospheric Chemistry and Physics*, 20, 9281–9310, <https://doi.org/10.5194/acp-20-9281-2020>,  
1277 2020.

1278 Ukhov, A., Ahmadov, R., Grell, G., and Stenchikov, G.: Improving dust simulations in WRF-Chem  
1279 v4.1.3 coupled with the GOCART aerosol module, *Geosci. Model Dev.*, 14, 473–493,  
1280 <https://doi.org/10.5194/gmd-14-473-2021>, 2021.

1281 Yamashita, K.; Murakami, M.; Hashimoto, A.; Tajiri, T.: CCN Ability of Asian Mineral Dust Particles  
1282 and Their Effects on Cloud Droplet Formation, *Journal of Meteorological Society of Japan*, 89,  
1283 581–587, 2011.

1284 Yang, Q., W. I. Gustafson Jr., Fast, J. D., Wang, H., Easter, R. C., Morrison, H., Lee, Y.-N., Chapman, E.  
1285 G., Spak, S. N., and Mena-Carrasco, M. A.: Assessing regional scale predictions of aerosols,  
1286 marine stratocumulus, and their interactions during VOCALS-REx using WRF-Chem,  
1287 *Atmospheric Chemistry and Physics*, 11, 11951–11975, [https://doi.org/10.5194/acp-11-11951-](https://doi.org/10.5194/acp-11-11951-2011)  
1288 [2011](https://doi.org/10.5194/acp-11-11951-2011), 2011.

1289 Yang, Q., Gustafson Jr., W. I., Fast, J. D., Wang, H., Easter, R. C., Wang, M., Ghan, S. J., Berg, L. K.,  
 1290 Leung, L. R., and Morrison, H.: Impact of natural and anthropogenic aerosols on stratocumulus  
 1291 and precipitation in the Southeast Pacific: a regional modelling study using WRF-Chem,  
 1292 *Atmospheric Chemistry and Physics*, 12, 8777–8796, <https://doi.org/10.5194/acp-12-8777-2012>,  
 1293 2012.  
 1294 Yanlong Tai, Haoran Liang, Abdelali Zaki, Nabil El Hadri, Ali M. Abshaev, Buzgigit M. Huchunaev,  
 1295 Steve Griffiths, Mustapha Jouiad, and Linda Zou, *ACS Nano*, 11(12), 12318–12325,  
 1296 <https://doi.org/10.1021/acsnano.7b06114>, 2017.  
 1297 Yin, Y. and Chen, L.: The effects of heating by transported dust layers on cloud and precipitation: a  
 1298 numerical study, *Atmospheric Chemistry and Physics*, 7, 3497–3505. [https://doi.org/10.5194/acp-](https://doi.org/10.5194/acp-7-3497-2007)  
 1299 [7-3497-2007](https://doi.org/10.5194/acp-7-3497-2007), 2007.  
 1300 Yin, Y., Wurzler, S., Levin, Z., and Reislin, T. G.: Interactions of mineral dust particles and clouds:  
 1301 Effects on precipitation and cloud optical properties, *Journal of Geophysical Research*, 107(D23),  
 1302 4724, doi:[10.1029/2001JD001544](https://doi.org/10.1029/2001JD001544), 2002.  
 1303 Zaveri, R. A. and Peters, L. K.: A new lumped structure photochemical mechanism for large-scale  
 1304 applications, *Journal of geophysical Research*, 104, 30387–30415.  
 1305 <https://doi.org/10.1029/1999JD900876>, 1999.  
 1306 Zaveri, R. A., Easter, R. C., Fast, J. D., and Peters, L. K.: Model for Simulating Aerosol Interactions and  
 1307 Chemistry (MOSAIC), *Journal of geophysical Research*, 113, D13204,  
 1308 <https://doi.org/10.1029/2007JD008782>, 2008.  
 1309 Zeinab S., Z., Steiner, A., Zakey, A. S., Shalaby, A. and Wahab, M. M. A.: An exploration of the aerosol  
 1310 indirect effects in East Asia using a regional climate model, *Atmósfera*, 33(1), 87–103,  
 1311 <https://doi.org/10.20937/ATM.52604>, 2020.  
 1312 Zhang, Y., Wang, K. and He, J.: Multi-year application of WRF-CAM5 over East Asia-Part II:  
 1313 Interannual variability, trend analysis, and aerosol indirect effects, *Atmospheric Environment*,  
 1314 165, 222–239, <https://doi.org/10.1016/j.atmosenv.2017.06.029>, 2017.  
 1315 Zhang, Y., He, J., Zhu, S., and Gantt, B.: Sensitivity of simulated chemical concentrations and aerosol-  
 1316 meteorology interactions to aerosol treatments and biogenic organic emissions in WRF/Chem,  
 1317 *Journal of Geophysical Research: Atmosphere*, 121, 6014– 6048,  
 1318 <https://doi.org/10.1002/2016JD024882>, 2016.  
 1319 Zhao, B., Wang, Y., Gu, Y., Liou, K. –N., Jiang, J. H., Fan, J. et al.: Ice nucleation by aerosols from  
 1320 anthropogenic pollution, *Nature Geoscience*, 12, 602–607, [https://doi.org/10.1038/s41561-019-](https://doi.org/10.1038/s41561-019-0389-4)  
 1321 [0389-4](https://doi.org/10.1038/s41561-019-0389-4), 2019.  
 1322 Zhao, C., Liu, X., Ruby Leung, L., and Hagos, S. (2011). Radiative impact of mineral dust on monsoon  
 1323 precipitation variability over West Africa. *Atmospheric Chemistry and Physics*, 11, 1879–1893.  
 1324 <https://doi.org/10.5194/acp-11-1879-2011>, 2011.  
 1325 Zhao, C., Liu, X., Leung, L. R., Johnson, B., McFarlane, S. A., Gustafson Jr., W. I. et al.: The spatial  
 1326 distribution of mineral dust and its shortwave radiative forcing over North Africa: modeling  
 1327 sensitivities to dust emissions and aerosol size treatments, *Atmospheric Chemistry and Physics*,  
 1328 10, 8821–8838, <https://doi.org/10.5194/acp-10-8821-2010>, 2010.